sid.inpe.br/mtc-m21d/2021/07.21.11.33-TDI

SPACE WEATHER EFFECTS ON THE BRAZILIAN EQUATORIAL SPREAD F: OBSERVATION AND IRI MODEL

Samuel Abaidoo

Master's Dissertation of the Graduate Course in Space Geophysics, guided by Drs. Claudia Maria Nicoli Cândido, and Fábio Becker Guedes, approved in June 28, 2021.

URL of the original document:
<http://urlib.net/8JMKD3MGP3W34T/4559JM2>

INPE
São José dos Campos
2021

PUBLISHED BY:

Instituto Nacional de Pesquisas Espaciais - INPE
Coordenação de Ensino, Pesquisa e Extensão (COEPE)
Divisão de Biblioteca (DIBIB)
CEP 12.227-010
São José dos Campos - SP - Brasil
Tel.:(012) 3208-6923/7348
E-mail: pubtc@inpe.br

BOARD OF PUBLISHING AND PRESERVATION OF INPE INTELLECTUAL PRODUCTION - CEPPII (PORTARIA Nº 176/2018/SEI-INPE):

Chairperson:

Dra. Marley Cavalcante de Lima Moscati - Coordenação-Geral de Ciências da Terra (CGCT)

Members:

Dra. Ieda Del Arco Sanches - Conselho de Pós-Graduação (CPG)

Dr. Evandro Marconi Rocco - Coordenação-Geral de Engenharia, Tecnologia e Ciência Espaciais (CGCE)

Dr. Rafael Duarte Coelho dos Santos - Coordenação-Geral de Infraestrutura e Pesquisas Aplicadas (CGIP)

Simone Angélica Del Ducca Barbedo - Divisão de Biblioteca (DIBIB)

DIGITAL LIBRARY:

Dr. Gerald Jean Francis Banon

Clayton Martins Pereira - Divisão de Biblioteca (DIBIB)

DOCUMENT REVIEW:

Simone Angélica Del Ducca Barbedo - Divisão de Biblioteca (DIBIB)

André Luis Dias Fernandes - Divisão de Biblioteca (DIBIB)

ELECTRONIC EDITING:

Ivone Martins - Divisão de Biblioteca (DIBIB)

André Luis Dias Fernandes - Divisão de Biblioteca (DIBIB)

sid.inpe.br/mtc-m21d/2021/07.21.11.33-TDI

SPACE WEATHER EFFECTS ON THE BRAZILIAN EQUATORIAL SPREAD F: OBSERVATION AND IRI MODEL

Samuel Abaidoo

Master's Dissertation of the Graduate Course in Space Geophysics, guided by Drs. Claudia Maria Nicoli Cândido, and Fábio Becker Guedes, approved in June 28, 2021.

URL of the original document:
<http://urlib.net/8JMKD3MGP3W34T/4559JM2>

INPE
São José dos Campos
2021

Cataloging in Publication Data

Abaidoo, Samuel.

Ab15s Space weather effects on the brazilian equatorial spread F: observation and IRI model / Samuel Abaidoo. – São José dos Campos : INPE, 2021.

xxii + 84 p. ; (sid.inpe.br/mtc-m21d/2021/07.21.11.33-TDI)

Dissertation (Master in Space Geophysics) – Instituto Nacional de Pesquisas Espaciais, São José dos Campos, 2021.

Guiding : Drs. Claudia Maria Nicoli Cândido, and Fábio Becker Guedes.

1. Equatorial ionosphere. 2. Equatorial spread-F. 3. Solar wind. 4.Digisonde. 5. Solar minimum. I.Title.

CDU 550.388.2

Esta obra foi licenciada sob uma Licença Creative Commons Atribuição-NãoComercial 3.0 Não Adaptada.

This work is licensed under a Creative Commons Attribution-NonCommercial 3.0 Unported License.

MINISTÉRIO DA CIÊNCIA, TECNOLOGIA E INOVAÇÕES

INSTITUTO NACIONAL DE PESQUISAS ESPACIAIS

DEFESA FINAL DE DISSERTAÇÃO DE SAMUEL ABAIDOO
BANCA Nº 181/2021 REG 11993/2019

No dia 28 de junho de 2021, as 09h00min, por teleconferência, o(a) aluno(a) mencionado(a) acima defendeu seu trabalho final (apresentação oral seguida de arguição) perante uma Banca Examinadora, cujos membros estão listados abaixo. O(A) aluno(a) foi APROVADO(A) pela Banca Examinadora, por unanimidade, em cumprimento ao requisito exigido para obtenção do Título de Mestre em Geofísica Espacial / Ciências Atmosféricas. O trabalho precisa da incorporação das correções sugeridas pela Banca Examinadora e revisão final pelo(s) orientador(es).

Novo título: "Space weather effects on the Brazilian equatorial spread-F during solar minimum: observations and IRI model"

Membros da banca:

Dr. Marcelo Magalhães Fares Saba - Presidente - INPE
Dra. Claudia Maria Nicoli Cândido - Orientadora – INPE
Dr. Fábio Becker Guedes - Orientador - INPE
Dr. Siomel Savio Odriozola - Membro Interno - INPE
Dra. Virgínia Klausner - Membro Externo - UNIVAP

Documento assinado eletronicamente por **CLAUDIA MARIA NICOLI CANDIDO (E)**, **Usuário Externo**, em 06/07/2021, às 13:18 (horário oficial de Brasília), com fundamento no § 3º do art. 4º do Decreto nº 10.543, de 13 de novembro de 2020.

Documento assinado eletronicamente por **Marcelo Magalhães Fares Saba**, **Pesquisador**, em 09/07/2021, às 10:11 (horário oficial de Brasília), com fundamento no § 3º do art. 4º do Decreto nº 10.543, de 13 de novembro de 2020.

Documento assinado eletronicamente por **Fábio Becker Guedes**, **Pesquisador**, em 12/07/2021, às 10:06 (horário oficial de Brasília), com fundamento no § 3º do art. 4º do Decreto nº 10.543, de 13 de novembro de 2020.

Documento assinado eletronicamente por **Siomel Savio Odriozola (E)**, **Usuário Externo**, em 17/07/2021, às 13:26 (horário oficial de Brasília), com fundamento no § 3º do art. 4º do Decreto nº 10.543, de 13 de novembro de

2020.

Documento assinado eletronicamente por **Virginia Klausner de Oliveira (E)**, **Usuário Externo**, em 22/07/2021, às 15:49 (horário oficial de Brasília), com fundamento no § 3º do art. 4º do Decreto nº 10.543, de 13 de novembro de 2020.

A autenticidade deste documento pode ser conferida no site http://sei.mctic.gov.br/verifica.html, informando o código verificador **7772200** e o código CRC **4DB926A8**.

Referência: Processo nº 01340.004166/2021-40 SEI nº 7772200

ACKNOWLEDGEMENTS

I am most indebted to the almighty God for his superior oversight, without which I would not have made it to this threshold. I wish to express my unflinching appreciation to all who in diverse ways have contributed immensely to this research work especially my noble institute; National Institute for Space research (INPE) and CNPq by the financial support. My profound gratitude also goes to my Advisors Dr. Claudia M N Candido and Dr. Fabio Becker Guedes, God richly blesses you for your vast reserve of patience and knowledge. Lastly, I express deep gratitude to Michael Obiri Yeboah, Kayoko Tochigi Yeboah and Michael Tochigi for all the diverse support contributed to my life, I say God bless you all. Finally, thank my parent for their words of wisdom and inspiration.

ABSTRACT

This work present the study of the Brazilian Equatorial spread-F during the solar minimum year,2018. For this purpose, ionospheric data obtained by a Digisonde installed in Belem, PA (BL; 48°W, 1.43°S; Dip: -2.6°) were analyzed. Spread-F is the generic term referring to plasma density fluctuations in the ionospheric F-region after sunset. Its importance is attributed to its effects on the radio waves propagation between satellites and ground-based receivers, which in its turn affect global navigation and positioning systems. In the Brazilian sector, characterized by a large negative declination angle of magnetic equator, it is observed a high occurrence of equatorial spread-F/equatorial plasma bubbles. The interest on to study spread-F on solar minimum is that there are no intense geomagnetic disturbances. In general, weak-to-moderate storms mostly driven by High-Speed Solar wind streams, HSSs, and Corotating Interaction region, CIRs occurr. These storms are weaker than those driven by Coronal Mass Ejections, CMEs. However, they present a long-duration recovery phase. This "quiescent" scenario provides good conditions to analyze the ionospheric response. The equatorial spread-F occurrence rate was determined after analyzing thousands of ionograms provided by the Digisonde installed at Belem and a statistical study of was performed. At first, the spread-F was classified in three main patterns: Range, Frequency, and Mixed spread-F. The start time and duration of spread-F were also evaluated for each night of the year. It was observed a seasonal variation, with peaks in Summer solstice and Equinoxes, and a minimum occurrence in June Solstice. The onset time was mostly at around 21:00 LT, and it was noticed that spread-F duration time is higher in Summer and Equinoxes than in June Solstice. The spread-F probability was additionally calculated by the IRI model for each hour in each month. It was noticed that there is a similar trend for observed and calculated probability. However, some some discrepancies were observed during disturbed intervals: IRI model may underestimate or overestimate the spread-F probability. The spread-F day-to-day variability was also considered. It was observed that spread-F during solar minimum can occur during quiet or disturbed geomagnetic intervals with variable duration. However, under some moderate disturbed conditions, spread-F can be suppressed or favored. In this way, the influence of a moderate geomagnetic storm on the equatorial F-region heights and frequencies was carefully investigated by the analyzes of ionospheric parameters such as the virtual F-layer height, h^IF; the F-layer peak height, hmF2, and the critical plasma frequency, foF2. It was selected a disturbed geomagnetic interval in May, a month considered out of the 'Spread-F season" in Brazil for a study case. It was observed that during the main phase of the storm, the F-region experienced a sudden uplift associated with an intensified ExB vertical drift at nighttime. This uplift was probably caused by enhanced zonal electric field associated to a Prompt Penetration of Electric Field, PPEF. In its turn, the plasma density was intensified over its five quietest days average, 5QD, for some days of the recovery phase. These finding can contribute to a better understanding of the ionosphere during solar minimum a to Space Weather prediction programs.

Keywords: Equatorial ionosphere. Equatorial spread-F. Solar wind. Digisonde. Solar minimum. Space weather. IRI model.

EFEITOS DO CLIMA ESPACIAL NA PROPAGAÇÃO EQUATORIAL BRASILEIRA F: MODELO DE OBSERVAÇÃO E IRI

RESUMO

Este trabalho apresenta o estudo do spread-F equatorial na região brasileira durante o mínimo solar 2018. Para tanto, foram analisados dados ionosféricos obtidos por uma Digissonda instalada em Belém, PA (BL; 48°W, 1.43°S; Dip: -2.6°). Spread-F é o termo genérico que se refere às flutuações da densidade do plasma na região F ionosférica após o pôr do sol, as chamadas irregularidades do plasma ionosférico equatorial, ou Bolhas de plasma eqautoriais. Sua importância se deve aos seus efeitos na propagação das ondas de rádio entre satélites e receptores terrestres, e portanto, nos sistemas globais de navegação e posicionamento. No setor brasileiro, caracterizado por um grande ângulo de declinação negativo do equador magnético, observa-se uma alta taxa de ocorrência de spread-F/bolhas de plasma equatorial. Neste trabalho estuda-se o spread-F eqautorial durante um ano de mínimo solar,o qual é caracterizado pelo baixo número de manchas e regiões ativas no Sol, bem como valores menores de fluxo solar. Neste periodo, tempestades geomagnéticas intensas não são esparsas, enquanto tempestades fracas a moderadas são frequentes. Tais tempestades geomagnéticas são principalmente geradas por fluxos de vento solar de alta velocidade, HSSs (High-Speed Solar Wind Streams), e regiões de interação corrotante, CIRs (Corotating Interaction Regions). Embora essas tempestades sejam menos intensas do que as provocadas por Ejeções de Massa Coronal, CMEs (Coronal Mass Ejections), elas apresentam uma fase de recuperação de longa duração (vários dias), o que causa respostas ionosféricas de longa duração. A taxa de ocorrência do spread-F equatorial foi realizado após a análise de milhares de ionogramas fornecidos pela Digissonda instalada em Belém. O spread-F foi classificado em três padrões principais: Range, Frequency e Misto (uma combinação de ambos). Características como a hora de início e fim e a duração do spread-F foram avaliadas para cada noite do ano. O estudo estatistico mostrou que há uma uma variação sazonal, com picos de ocorrência entre os equinõcios no hemisfério sul, e mínimo durante o solstício de inverno. Em geral, o horário de início do spread-F foi principalmente por volta das 21:00 hora local. Adicionalmente, observou-se que que o tempo de duração do spread-F foi maior durante os meses de verão e equinócios do que no solstício de inverno. A probabilidade de ocorrência do Spread-F foi calculada baseada nas observações e foi calculada pelo modelo IRI para cada mês. Observou-se que existe uma tendência similar para as probabilidades observada e a calculada, embora com algumas discrepâncias do modelo IRI, o qual pode subestimar ou superestimar o spread-F observado especialmente em periodos perturbados. A variabilidade diária do spread-F também foi considerada na análise. Foi observado que o spread-F durante o mínimo solar pode ocorrer durante períodos geomagneticamente calmos ou perturbados, com duração variável. No entanto, sob algumas condições geomagneticamente moderadas, o spread-F pode ser favorecid em periodos não usuais. A influência de uma tempestade geomagnética moderada no spread-F foi investigada pela análise de parâmetros ionosféricos como a altura virtual da camada F, h^IF, a altura do pico da camada F, hmF2 e a frequência crítica do plasma, foF2. O intervalo geomagneticamente perturbado foi o mês de maio, um mês considerado fora da

"temporada de spread-F" no Brasil. Foi percebido que durante a fase principal da tempestade a região F experimentou uma elevação rápida associada a uma intensificação do campo eletrico e consequentemente da deriva vertical ExB durante a noite, provavelmente causada por um episódio de penetração súbita de campo elétrico, PPEF (Prompt Penetration Electric Field). Além disso, a frequencia/densidade do plasma foi intensificada acima da média dos cinco dias mais calmos de maio (5QD) durante a fase de recuperação. Estes resultados podem contribuir para estudos dos efeitos de Clima Espacial em baixa atividade solar.

Palavras-chave: Ionosfera equatorial. Equatorial spread-F. vento solar. Mínimo solar. Clima Espacial. Modelo IRI.

LIST OF FIGURES

Page

LIST OF TABLES

Page

LIST OF ABBREVIATIONS

AU	–	Astronomical Unit
BL	–	Belem
B	–	Interplanetary Magnetic Field
CMEs	–	Coronal Mass Ejection
CRT	–	Collisonal Rayleigh-Taylor
CIRs	–	Corotating Interaction Regions
DDEFs	–	Disturbance Dynamo Electric Fields
DPS	–	Digisonde Portable Sounder
EIA	–	Equatorial ionization anomaly
ESF	–	Equatorial Spread-F
EPBs	–	Equatorial Plasma Bubbles
EUV	–	Extreme Ultraviolet Radiation
FSF	–	Frequency Spread F
FAIs	–	Field Aligned Irregualrities
FZ	–	Fortaleza
GNSS	–	Global Navigation Satellite System
GRT	–	General Rayleigh-Taylor
GPS	–	Global Position System
GWs	–	Gravity waves
GICs	–	Geomagnetic Induced Currents
HSWS	–	High Solar Wind Speeds
IMF	–	Interplanetary Magnetic Field
IRI	–	International Reference Ionosphere - IRI-2012
IMF	–	Interplanetary magnetic field
kp	–	Geomagnetic Index
LSTIDs	–	Large Scale TIDs
LT	–	Local time
MSTIDs	–	Medium Scale TIDs
MSF	–	Mixed Spread F
MUF	–	Maximum usuable frequency
ND	–	No Digisonde (no data acquisition by Digisonde)
NT	–	Number of Occurrence in Each Time
PPEF	–	Prompt Penetration of Electric Field
PMIs	–	Postmidnight plasma irregularities
PRE	–	Pre-reversal Enhancement
PPEF	–	Prompt Penetration Electric Field
5QD	–	Quiest day
RSF	–	Range Spread F
RT	–	Rayleigh–Taylor
SL	–	São Luís
SIDs	–	Ionospheric Disturbances
SFU	–	Solar Flux Unit
SSTIDs	–	Small Scale TIDs

Sym H	–	Ring Current Index
SF	–	spread-F
TEC	–	Total Electron Content
TM	–	Total Number of Spread F in Month
UT	–	Universal time
URSI	–	Union Radio-Scientifique Internationale
Vsw	–	Solar Wind Speed

LIST OF SYMBOLS

γ	–	growth rate of the instability
$\varepsilon_\circ$	–	electrical permittivity in a vacuum
Å	–	Amstrong
ω	–	conductivity
B	–	terrestrial magnetic induction field
E	–	zonal electric field
e	–	charge of the electron
f	–	frequency of the electromagnetic wave
F_n	–	frequency of the plasma
g	–	gravitational acceleration
$\overline{\sigma_H}$	–	Hall conductivty
Ω_i	–	ion gyro-frequency
V_{in}	–	ion-neutral collision frequency
J	–	Current
L	–	Plasma scale length
m_e	–	electron mass
m_i	–	ion mass
m	–	mass of the electron
Ne	–	electronic density
e	–	electrical charge
μ	–	refractive wave index
x	–	ordinary wave
y	–	extraordinary wave
V_D	–	Zonal Drift
λ	–	Wave lenght
W_x	–	Zonal wind
W_z	–	vertical wind
n_{io}	–	electron density
$\overline{\sigma_P}$	–	Pedersen conductivity

CONTENTS

Page

1 INTRODUCTION

The ionosphere is defined by (HAYMES, 1971) as a layer of the Earth's atmosphere, characterized mainly by the presence of partially ionized gases and electrically charged by the action of solar radiation in EUV. This layer is located approximately between 60 and 1000 km height and is subdivided into regions, according to the electron density and the local chemical composition. The ionosphere is a dispersive medium through which signals of different frequencies travel at slightly different velocities. At the lowest altitudes, it also tends to absorb radio waves rather than reflect them, all these characteristics cause a variety of effects on propagating electromagnetic signals. In other words, it is a region where the quantity of existing ions and electrons is enough to affect the propagation of radiowaves signals.

The diurnal ionosphere is divided into D, E and F layers. The F layer is usually subdivided into F1 and F2, although a third layer, near the magnetic equator and was named the F3 layer. The ionosphere is not a uniform plasma region. Its density changes with: the time of day, altitude, latitude, season, solar activity, geomagnetic activity, and can be affected by wave activity from lower heights. These conditions result in a F layer plasma density profile which may become unstable to interchange instability and cause high depleted plasma density magnetic flux tubes at the bottom side of the ionospheric F region in a situation analogous to the hydrodynamic Rayleigh-Taylor: heavy fluid over light fluid instability. These plasma instabilities occur over a broad range of time and length scales due to the combined effects of chemical recombination and an increase in the vertical plasma velocity leading the development of plasma irregularities. Plasma irregularities are fluctuation in the plasma density observed such as patches, clumps, depletions, and troughs of ionization (KELLEY, 2009). Early ground-based investigations of the ionosphere observed diffuse echoes in data from measurements using high frequency radars named ionosondes (BREIT; TUVE, 1926; BOOKER; WELLS, 1938; BERKNER; WELLS, 1934; ABDU et al., 1998). This phenomenon is now generically known as Equatorial Spread-F (ESF).

Equatorial spread-F is a phenomenon in which the equatorial ionosphere is reshaped after sunset and it was first reported by (BERKNER, 1930) at Huancayo, Peru. Over the equatorial region, around sunset times the circulation system with the thermospheric wind blowing eastward, in the presence of the abrupt decay of the E region conductivities and the quasi horizontal geomagnetic field, produces a Pre Reversal Enhancement in the evening zonal electric field (PRE) resulting in a sharp

vertical E×B drift of F layer. The rapid vertical drift of the post sunset F layer in presence of seeding processes can result in instability growth (Rayleigh-Taylor instability) leading to large-scale field aligned plasma depletions, known as equatorial plasma bubbles, EPBs, with associated cascading irregularities constituting a spread-F event. As these depletions vertically develop to higher altitudes over the equator (attaining altitudes of one or two thousand kilometers) they are transported as depleted tube flux, by effects of diffusion, pressure gradients and gravity to higher latitudes (ABDU et al., 2003). Their scale is from 10's of centimeters to 100's of kilometers (ABDU et al., 2009). The spread-F is globally observed from equatorial region to auroral latitudes, over all the longitudinal sectors of the Earth and their occurrence depends on several factors. The spread-F is divided in two main types: the frequency spread-F and the range spread-F. The former is observed at the higher-frequency end of the ordinary and extraordinary traces in the ionograms, being associated to plasma density irregularities near the F layer peak. The later is usually interpreted as the spread of multiple echoes coming from oblique directions out of zenithal region. The most favorable conditions for the ESF/EPBs occur during high solar activity periods, between September and March, presenting its lowest occurrence rate of ∼10% during June solstice according to (SOBRAL et al., 2002) and to (KOGA et al., 2011). These irregularity structures can cause amplitude and phase scintillation of the propagating signals, thereby compromising the availability, performance, and integrity of satellite-based communication and navigation systems. This work aims to investigate the spread-F features during solar minimum activity in 2018. During this period, spread-F may be affected by the occurrence of moderate geomagnetic storms, associated with Solar Wind High-Speed Streams, HSSWSs, and Corotating Interation Regions, CIRs. Additionally, the ionospheric IRI model was used to assess the spread-F probability in comparison to the observations.

1.1 Motivation

The present work aims to understand the Equatorial spread-F, the ionospheric variability during solar minimum 2018 and the possible influence of moderate geomagnetic storms associated with Solar Wind High Speed Streams on its features and development.

1.2 Why to study Equatorial Spread F during Solar Minimum

- During solar minimum the Solar Wind is slower and less variable than other periods;

- The interplanetary medium is less “energized”;
- Solar minimum is the perfect time to characterize the “baseline” system;
- A good understanding of the solar minimum can help to construct a better understanding of the more active intervals Gibson, 2019

1.3 Objectives

The objectives of this study are:

General: To study the Equatorial Spread-F Occurrences Pattern/Rate during solar minimum conditions.

Specific:

- Identify and classify the different patterns of spread F during solar minimum activity over the equatorial region ;
- To perform a statistical study of the equatorial spread F during solar minimum;
- To examine the start time and end time of the different types of Equatorial Spread F events;
- To examinate the possible influence of moderate geomagnetic storms on the spread-F;
- To examine spread-F probability using IRI model in comparison to the observations.

2 THE IONOSPHERE

The upper atmosphere comprises of the mesosphere, thermosphere, exosphere, and the ionosphere as part of the portion to be distinguished due to its ionized nature. It plays an essential role in atmospheric electricity and performs the inner edge of the magnetosphere. It's essential because of its influence on radio waves as a passage medium to a distinct part of the globe. Marconi Trans-Atlantic radio wave propagation experiment conducted in 1901 inferred the atmosphere. In 1902, Kennelly and Heaviside further hypothesized the existence of an ionized layer around the Earth that could guide the electromagnetic waves to greater distances and was named the Heaviside layer (named after the physicist Oliver Heaviside) but later replaced by Robert Watson-Watt during 1926 as the ionosphere. This really provided much knowledge about the ionosphere until the age of rockets and satellites began in the I940 and 1950's. Though tremendous amount of research works have been devoted to studies of the ionosphere, nevertheless, for more than a century after its discovery, the Earth's ionosphere still remains a poorly explored region. Still, scientific community is unable to predict the ionospheric behavior precisely, either during geomagnetic storms, or during geomagnetically quiet time conditions.

2.1 The structure and composition of the Earth´s ionosphere

The understanding of the structure and dynamics of the ionospheric plasma at a specific period is indispensable for various scientific applications and services, such as telecommunication via radio signals, point positioning based on global navigation satellite systems (GNSS). The ionosphere is composed of two main layers: the lower layer, normally designated as layer E and is sometimes also known as Heaviside or Kennelly-Heaviside layer located between 80 and 130 km beyond the Earth's surface reflecting low-frequency radio waves; and the upper layer, also known as F or Appleton layer, which reflects higher frequency radio waves which in turn is divided into F1 layer, which begins about 180 km above the ground; and the F2 layer, which emerges about 300 km from the surface composing of electrons and positively charged ion, which makes it have a tenuous gas and a plasma. The diversity of physical, chemical and dynamical processes in the ionosphere leads to the formation of distinct heights and layers indicated by D, E, F1, and F2 due to the redistribution during ionization shown in Figure 2.1. The three prevailing components in the ionosphere are N_2, O_2 and O that are ionized by solar radiation to produce N_2^+, O_2^+, N^+, O^+ and NO^+ (KELLEY, 2009).

The D region is the lower part of the ionosphere, situated between 60-90 km, is pro-

Figure 2.1 - Vertical structure of the Earth's ionosphere and respective ionization sources in each altitude region as well as distribution of major ions.

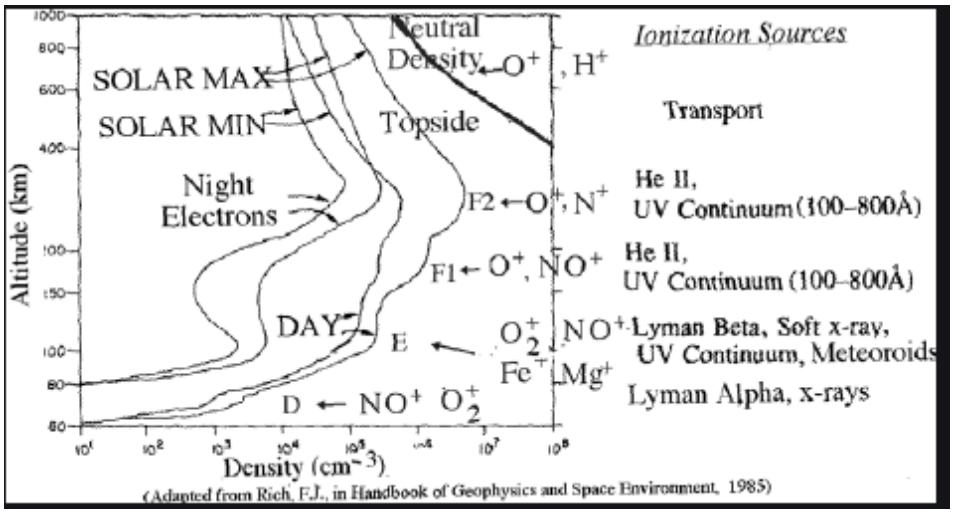

SOURCE: Kelley (2009).

duced by the most penetrating ionizing radiations which are generally very sensitive to solar activity. Solar L-alpha (121.6nm) radiation seems to be the most important for ionizing NO, solar X-rays (<0.8nm) for ionizing N_2, O_2 and Ar, solar ultraviolet (UV) radiation ($\lambda < 111.8$ nm) for ionizing unstable O_2, and galactic cosmic rays for ionizing all the constituents in D-layer (KELLEY, 2009). The maximum daytime density ranges from 10^2 to 10^4 cm^{-3}. The most important chemical reactions include the O, O_3, O_2, NO_2, CO_2 and H_2O.

The region E (Kennelly -Heaviside Layer) extends between regions D and F, approximately between 80 and 130 km of height, formed by the X-ray ionization with a wavelength in the range 10Å $< \lambda <$ 100Å and by L_y B (= 1025Å) radiation. The predominant ions are O_2^+ and NO^+.The peak density is of the order of 10^5 cm^{-3}. The ionization is due to soft X-rays (1-10nm) and far-ultraviolet (UV)solar radiation ionization of molecular oxygen O_2. The competing effects of ionization and recombination primarily define the vertical structure of the E layer. Metallic ions such as Fe^+, Mg^+, Na^+, K^+, Ni^+ and Si^+ have also been discovered to form a thin layer called sporadic E within the E-region produce by neutral atoms precipitation by meteors that become ionized by photoionization or exchange of charges with ions existing in the ionosphere. The metallic ions have a more lasting existence than the molecular ions of the E-region, hence persisting during the night once is

formed (KELLEY, 2009)

The F region (Appleton–Barnett layer) extends from about 150 km to more than 500 km above the surface of Earth for which UV radiation is the predominant ionization source. The F1 layer is a transition region between molecular ions O_2^+ and NO^+ below and atomic ions O^+ above. It lies between 140 and 600 km. the F1 layer is more pronounced in summer than in winter, always disappears during the night. The main source of ionization is extreme ultraviolet (EUV) solar radiation in the wavelengths $\lambda \approx 58.4$ and 30.4 nm (KELLEY, 2009). The F2 layer is very complex and depends on magnetic latitude having an average peak electron density around 300 km with a maximum density of the order of 160 cm^{-3} and exhibits dependence on solar zenith angle and sunspot number. The region below and above the F2 peak is called the bottom-side and topside ionosphere respectively where diffusion is the dominant process, and the vertical distribution of electrons cannot be described solely in terms of the balance between production and loss.

In this region, the ratio of the collision to gyrofrequency for both ions and electrons are very low, thus making their velocities perpendicular to B nearly equal, hence uniquely defining plasma flow related to the electric field. The thermospheric wind system generated by the pressure inequalities in the solar EUV heating is the main driving force for the F-region dynamo.

The conductivity of the E region after sunset generates the F region dynamo (RISHBETH, 1971), hence forming a defined lower boundary of the F region as shown in the configuration Figure 2.2 for which the plasma is said to have a constant finite Pedersen conductivity inside the slab and zero outside, and a constant zonal wind (u) within the slab. The polarization electric fields in a vertical direction develop at the equatorial F-region giving rise to a zonal drift ($V_D = E \times B/B^2$) of the plasma, which is in the equal direction and magnitude to the neutral wind at nighttime (KELLEY, 2009).

Figure 2.2 - Electrodynamics of the equatorial F-region.

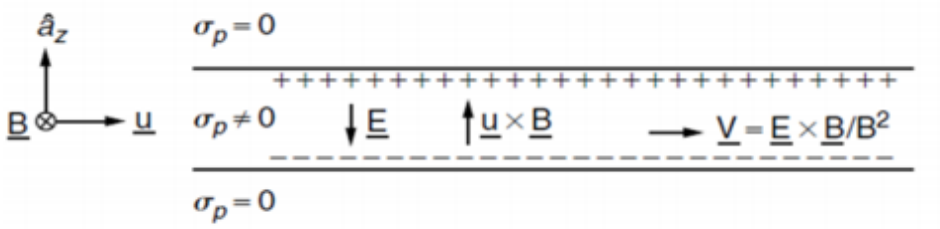

SOURCE: Kelley (2009).

Also the V_D, the charge separation occurs in such a way that the overall current (J_z) is zero. Thus ;

$$J_z = \sigma_p E_z + \sigma_p u B = 0 \tag{2.1}$$

This means that $E_z = -\mathbf{u} \times \mathbf{E} = -uB$. Thus, the perfect F-region dynamo can be generalized as,

$$E + U \times B = 0 \tag{2.2}$$

This indicate that electromagnetic force on the plasma disappears and the thermospheric wind blows loosely without ion drag during the nighttime.

Furthermore, the conductivity of the integrated E-region changes to that of the integrated F-region of the magnetic field line during the daytime processes making it impossible to build up the F-region field, and the daytime ion drag remains high Heelis et al. (1974).The magnitude of the zonal electric field is essentially determined by the winds in the E-region and the ionospheric conductivity during the day. Figure 2.3. illustrates the wind-driven current in the F-region and the E-region closure current that will result from any divergence in the F-region current.

$$E_z = \frac{(U(z)B)\Sigma_P^F(z)}{\Sigma_P^F + 2\Sigma_P^F(z)} \tag{2.3}$$

This model can be used to explain the general diurnal variation in the vertical electric field that maps E- to F-region.In the low-latitude F-region meridional winds have a prevailing element parallel to the magnetic field and thus do not drive a current since Hall conductivity is negligible, the Zonal which are predominantly perpendicular to the magnetic field, thus drive a current perpendicular to the wind and the magnetic field and vertical near the equator. The dashed lines illustrate field-aligned currents that complete the current loop. The F-region dynamo drives a current that is predominantly in the magnetic meridian due to the Pedersen conductivity. The electric polarization field in the magnetic meridian is given as :

$$\Sigma_F^P(E + U_F X B) = \Sigma_F^P E \tag{2.4}$$

When the horizontal current is divergent at the edges of the regions by assumption. Thus ,

$$E = \frac{\Sigma_F^P}{\Sigma_F^P + \Sigma_F^P}(U_F X B) \tag{2.5}$$

Hence describing the physical situation of the process .

In the daytime when the E-region Pedersen conductivity is so much larger than the F-region Pedersen conductivity the polarization field from this source is negligible but during the night time when the E-region Pedersen conductivity is essentially zero, the polarization field is directly proportional to the F-region dynamo wind.

The polarization, field is created by a divergence in the F-region current that results from altitude gradients in the Dux-tube integrated Pedersen conductivity. Fig.3 shows the local time distribution of the F-region zonal wind, which we assume is constant with altitude and latitude, and schematic distributions of the Dux-tube integrated Pedersen conductivity as function of Dux tube apex height for typical daytime and nighttime conditions. Signs on the nighttime profile indicate where polarization charges will accumulate to create the electric field.

This electric field will produce a dominant $E \times B$ zonal drift of the charged particles in the F-region. Furthermore, the polarization field will be the largest during the nighttime, when the E-region conductivity is smallest. Thus eastward nighttime drifts in the F-region will be larger than expectations based on consideration of the E-region dynamo winds only (RISHBETH, 1971).

Inclusion of the F-region dynamo therefore resolves one of the problems eluded to earlier, but does so by considering only the polarization ,eld in the magnetic meridian.The existence of the F3 layer(G-layer) between 500 km and 700 km altitude, depending on the phenomenon such as Equatorial Anomaly and the meridional wind.

Figure 2.3 - Current loop driven by zonal neutral winds in the F-region.

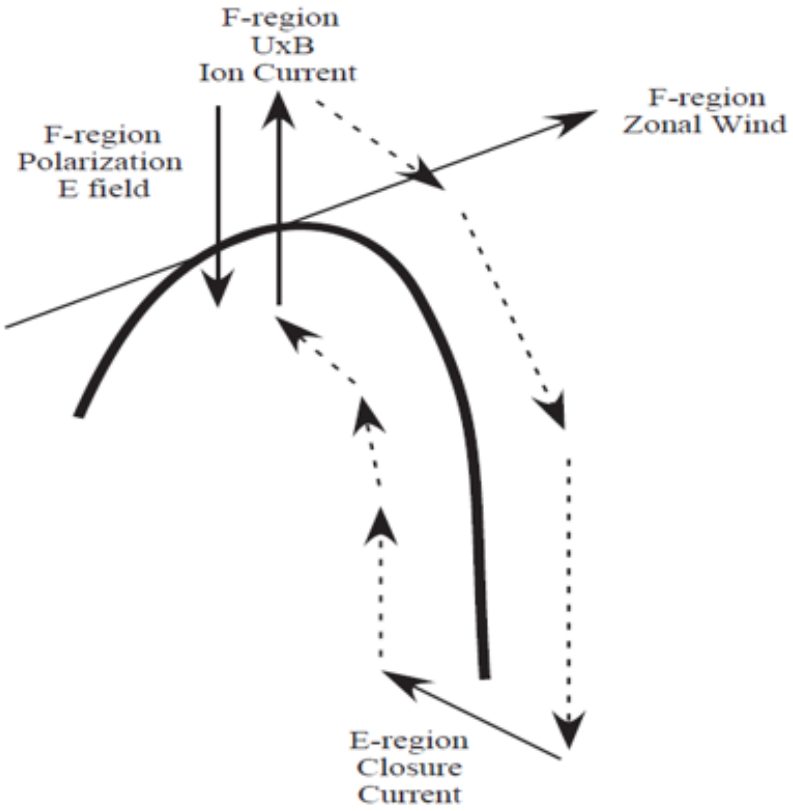

SOURCE: Heelis et al. (1974).

Figure 2.4 - Representative profiles of the total ion concentration during daytime and nighttime showing the peak and ledge of the F- and E-regions, respectively.

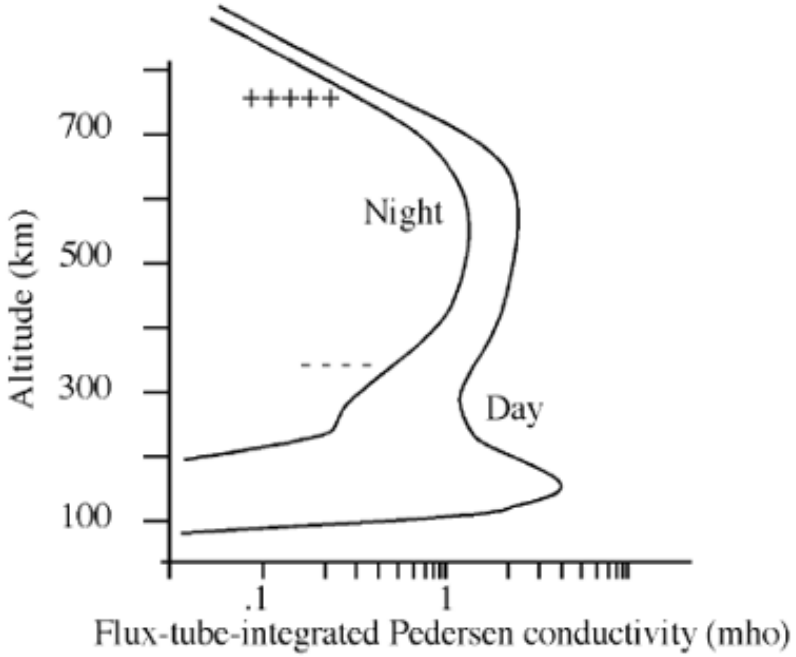

SOURCE: Heelis (2004)

2.2 The electrical conductivity of the ionosphere

In 1882, Balfour Stewart was the first to infer that the upper atmosphere is with significant electrical conductivity base on the solar daily geomagnetic variation. He considered that the cause of the electrical current to be in the upper atmosphere, not in the lower atmosphere or within the earth because these regions show no significant variation associated with the sunspot cycle. He further suggested the currents are produced by dynamo action, that is, by the movement of conducting air across the lines of force of the geomagnetic field, which makes the ionospheric conductivity an anisotropic.

The number of the charged particles, the electrical charge (e), mass(m), the mean collision frequency(v), and the gyrofrequency Ω_i in the presence of the magnetic field determine the conductivity of ionized gas. According to (RISHBETH, 1971), the electric currents of the ionosphere arise from interaction between the winds and

the magnetic field and through the electric fields that conduct ions and electrons in different directions. During the day, most part of the ionospheric current flows in region E, however, at night, with the fall ionization of that region, the dynamo of region F conducts most of the chain.In the ionosphere where both electric and magnetic fields are present, the conductivity is determined by the basic equations of motion for electrons and ions under the action of these fields (COWLING, 1945; BAKER, 1953; CHAPMAN, 1956). The three components of conductivity are; Parallel or longitudinal denoted as σ_{II}, this represents the electrical conductivity of theionosphere in the magnetic field direction and the same as when there is no magnetic field, Pedersen conductivities denoted as σ_P, which is the electrical conductivity of the ionosphere in the direction perpendicular to the magnetic field and the Hall conductivity denoted as σ_H this represent the electrical conductivity of the ionosphere in the direction perpendicular to both magnetic field and electric field. In the ionosphere, this conductivity is due to the drift motion of the electron ($E \times B$ drift) and maximum in the E region where the only electron practically drifts to the direction of $E \times B$. The height distributions of the Parallel, Pedersen, and Hall conductivities are subjected to the height distribution of the ion number density as shown in Figure 2.5. At night the conductivity in the E region is very slow as compared to the F region conductivity, in addition to this the Pedersen conductivity bears two peaks defining the daytime E and F region

The Hall conductivity is comparable to the Pedersen conductivity in the lower E-region but falls quickly with increasing height to become negligible compared to the Pedersen conductivity at about 200 km height. The parallel conductivity is much greater than the Pedersen and Hall conductivities at all heights we recognize enabling us to treat the magnetic field lines as nearly electric equipotentials.

Figure 2.5 - Altitude profiles of the direct conductivity SigO and the Hall and Pedersen conductivities SigH and SigP. Heavy curves denote daytime values; Lighter curves denote nighttime values.

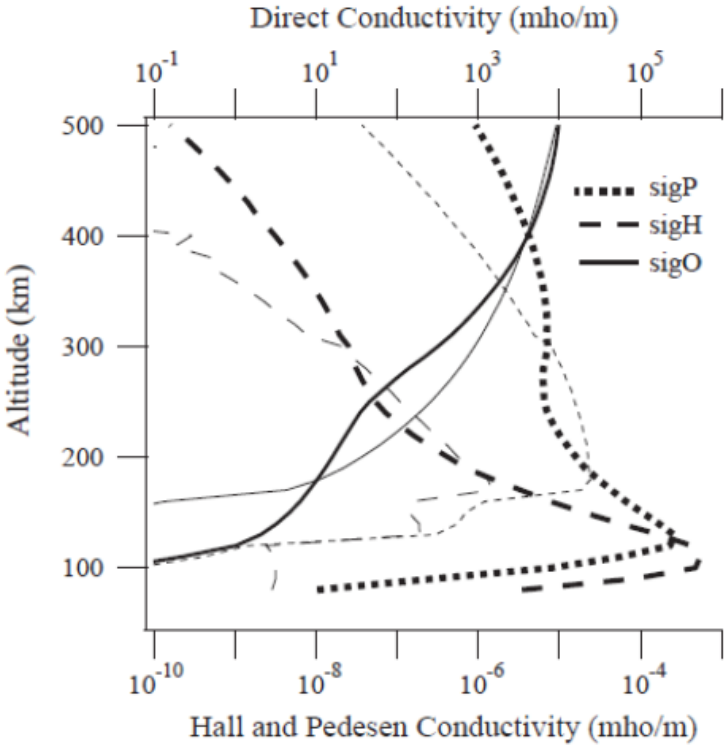

SOURCE: Heelis (2004).

Furthermore, their theoretical expressions are obtained from multifluid theory in which different charges and neutral species are treated as separate fluids that interact through collisions and are given as separate fluids that interact through collisions and are given as;

$$\delta_{II} = \frac{ne^2}{m_{eV_e}} \tag{2.6}$$

$$\delta_p = \frac{ne^2 V_{in}(V_e V_{in} + \omega_{ce}\omega_{ci})}{me(\omega_{ce}^2 V_{in}^2 + V_e^2 V_{in}^2 + \omega_{ce}^2\omega_{ci}^2)} \tag{2.7}$$

$$\delta_H = \frac{ne^2 V_{in}^2 \omega_{ce}}{me(\omega_{ce}^2 V_{in}^2 + V_e^2 V_{in}^2 + \omega_{ce}^2 \omega_{ci}^2)} \tag{2.8}$$

where V_{in}, and V_{en}, represent the effective collisional frequencies of the neutral particles with the electrons and the ions , e is the electron charge and defines as V_e= V_{ei}+ V_{en}V ; ω_{ce}= eB_o/m_e and ω_{ci}= $Z_e B_o/m_i$ are the gyro-frequencies of electrons and the ions respectively, with m_e and m_i denoting the electron and ion masses and z representing the ion charge state.

2.3 Ionospheric irregularities

Ionospheric phenomena known as spread-F are caused by instabilities within the ionosphere that allow plasma density irregularities to form.The irregularities exist at altitudes from 150 to 1000 km or even higher, with scale sizes ranging from tens of centimeters to hundreds of kilometers (ABDU et al., 1998). The equatorial and low latitude spread-F can occur from post-sunset until pre-dawn hours, usually happening at the beginning of the night. At these latitudes, the magnetic field **B** is nearly parallel to the Earth's and during daytime, the E-region dynamo electric field E is eastward. The resulting ExB drift transports the F region plasma upward at the magnetic equator. The uplifted plasma then moves along B lines in response to gravity and pressure gradient forces. As a result, the equatorial anomaly is formed with minimum F region ionization density at the magnetic equator and maxima at the two crests, approximately 15° – 20° in magnetic latitude to the north and south. These electrodynamics mechanism is known as the equatorial "fountain effect". Near sunset, plasma densities and dynamo electric fields in the E region decrease and the equatorial anomaly begins to weaken. However, at this local time, a dynamo develops in the F region. Polarization charges within conductivity gradients at the terminator enhance the eastward electric field after sunset. The post-sunset electric field moves the ionospheric plasma upward, allowing the equatorial anomaly crests to intensify. In these hours, a rapid uplifting of the F region and the steepening of the bottom side gradient lead to the Rayleigh-Taylor (R-T) instability (ABDU et al., 1981). The ionospheric irregularities are regions where the ionosphere electron density differs so significantly from the density of adjacent regions. This leads to a phenomenon called ionospheric scintillation, which is the rapid modification of radio waves caused by small-scale irregularities in the ionosphere. This term comes from the resemblance of ionospheric scintillation to the visible twinkling of stars in the night sky. That is, instead of a uniform layer of ionization, certain regions of the ionosphere are subject to patches of lower or higher density ionization. The phenomena arise from complex

physical processes, causing unwanted effects in transionospheric signals. Irregularities can be classified as positive or negative, according to the density difference. Abdu et al. (1981) report the occurrence of positive abnormalities, called "Plasma Blobs". However, the best known category includes the "Plasma Bubbles", which are regions where the electronic density decreases significantly due to depletion in the ionospheric plasma. The formation of bubbles occurs suddenly, from disturbances in the neutral atmosphere that propagate to the ionosphere. The plasma bubble phenomenon can last from minutes to several hours, and occurs mainly in the equatorial latitudes, where the ionosphere can present density differences of more than two orders of magnitude. Further, the irregularities can be exacerbated during geomagnetic storms Kelley (1989). During a storm development phase, electric fields promptly penetrate from auroral to equatorial latitudes with eastward polarity in the sunset sector, causing enhanced instability growth and hence leading to the development of the equatorial spread F (ESF), a feature that appears as a spread-F on the F-layer on ionograms. These irregularities preferentially form in two different regions over the Earth - the polar, or more correctly the auroral regions (both north and south), and the equatorial regions. In the Polar Regions, ionospheric irregularities are caused by particles precipitating down into the ionosphere from the magnetosphere (the same particles that produce the visible aurora). Flows of these particles cause bubbles and troughs, which are not stable, and at whose edges the scintillations are the strongest. Auroral scintillations may occur at any time of day, but tend to be stronger at night and when geomagnetic activity is high (i.e during geomagnetic storms). In the equatorial regions, after sunset, bubbles of ionization form at the bottom of the ionosphere and rise upward during the night forming vertical plumes (which can also be moving horizontally). Signals that propagate near the edges of these plumes are subject to the most intense scintillations. Equatorial scintillations are thus a nighttime phenomenon, with most of the plumes disappearing by midnight, although some do persist into the early morning hours. Equatorial scintillations increase in strength as the Sun's extreme ultra-violet (EUV) and X-ray output increases (which produces a thicker and more strongly ionized ionosphere). Thus, their intensity follows the approximately 11 year solar cycle. They also display a 27-day periodicity due to the solar rotation since the EUV producing plage is distributed unevenly across the solar surface.

2.4 Magnetosphere and ionosphere current system

The magnetosphere and ionospheric electrical currents flow more frequent due to the interaction of the terrestrial magnetic field with the solar wind. These currents define

the structure of the geomagnetic environment, which responds to a variety of external stimuli on a wide range of timescales. In addition, the size of the magnetosphere and the strength of the magnetopause currents that separate the interplanetary and terrestrial magnetic fields is affected by rapid changes in solar wind pressure. However, the variations in the strength and orientation of the interplanetary magnetic field (IMF) on timescales of minutes and hours control the level of interconnection between the interplanetary medium and the terrestrial field, modifying the structure of and circulation within the magnetosphere. The magnetic perturbations associated with currents flowing on the magnetopause, along magnetic field lines, in the ionosphere, and within the inner magnetosphere provide information regarding the dynamics of the magnetosphere. They also result in an extremely noisy magnetic environment that affect study of the internally produced magnetic field of the Earth. Several recent papers have reviewed the external electric current systems of the Earth and planets. (COWLEY, 2000) outlined the basic physical processes that give rise to current systems within the terrestrial solar wind–magnetosphere coupled system. (LOCKWOOD, 2013) provided an overview of the current systems and the geomagnetic indices which are used to monitor their intensity and variability, with the aim of determining changes in interplanetary conditions over the last dozen or so solar cycles (150 years or more).

A geomagnetic storm is a major disturbance of Earth's magnetosphere that occurs when there is a very efficient exchange of energy from the solar wind into the space environment surrounding Earth. These storms result from variations in the solar wind that produces major changes in the currents, plasmas, and fields in Earth's magnetosphere. During a geomagnetic storm the F2 layer will become unstable, fragment, and may even disappear completely. The primary causes of geomagnetic storms on Earth are strong dawn-to-dusk electric fields associated with the passage of southward-directed interplanetary magnetic fields, **BZ**, that pass the Earth for sufficiently long intervals of time. The solar wind energy transfer mechanism is magnetic reconnection between the IMF and the Earth's magnetic field. The electric field is composed of two factors: the solar wind velocity V and the southward IMF. It has been empirically shown by Gonzalez e Tsurutani (1987) that intense storms with peak Dst ≤ -100 nT are primarily caused by large **BZ** ≥ 10 nT fields with duration greater than 3 hours. Although such high fields are considerably greater than typical field magnitudes in the quiet solar wind (5 nT)(KING, 1986) and are therefore often associated with greater than average solar wind velocities (high-speed streams), it has been demonstrated that has a extraordinarily high **BZ**. The intense interplanetary magnetic fields can be thought of as being associated with essentially two parts

of a high-speed stream, the intrinsic fields, and plasma associated with the coronal ejecta (called driver gas fields), and the shocked and compressed fields and plasma due to the collision of the high-speed stream with the slower solar wind preceding it. In the latter case, the compression is related to the strength of the shock and thus to the speed of the high-speed stream relative to the upstream (slow) solar wind. The higher the relative velocity, the stronger the shock and the field being compressed (GONZALEZ et al., 1994).

The ionospheric variability is to a large extent driven by the solar and geomagnetic activity and is influenced by plasma transport, electric fields and currents, neutral winds and atmospheric waves (ABDU et al., 2009). The largest changes in regular ionospheric variability are usually caused by geomagnetic storms , which are triggered by the arrival of solar perturbations, such as coronal mass ejections (CMEs) and affect the entire magnetosphere. During storms, the currents in the ionosphere, as well as the energetic particles that precipitate into the ionosphere add energy in the form of heat that can increase the density and distribution of density in the upper atmosphere, causing extra drag on satellites in low-earth orbit. The local heating also creates strong horizontal variations in the ionospheric density that can modify the path of radio signals and create errors in the positioning information provided by GPS. While the storms create beautiful aurora, they also can disrupt navigation systems such as the Global Navigation Satellite System (GNSS) and create harmful geomagnetic induced currents (GICs) in the power grid and pipelines.

3 EQUATORIAL IONOSPHERE DYNAMICS

The purpose of the chapter is to present the Equatorial spread-F review and its electrodynamical process; The primary mechanism responsible for the generation of these irregularities including the seeding of MSTIDs and the gravity waves in the presence of the ionospheric plasma.

3.1 The Evening Enhancement

The motion of the equatorial ionosphere causes the plasma to move westward and upward during the day due to E×B drift and drift eastward and downward due to the reversal wind direction at nighttime. The dynamo effect of the E region neutral generates the electric field, which is minimal in the F region during the day. During the daytime, the zonal drift is negative and rises at night but at dusk, the vertical drift is positive preceding drift reversal at night and hence the name evening enhancement, or Prereversal Enhancement, of the equatorial ionospheric electrical field. Prereversal Enhancement is an Enhancement in the eastward electric field in the E-region of the ionosphere that is caused by a high conductivity gradient across the day-night terminator during the post-sunset hours Abdu et al. (1981). The dynamo effect by the F region, the neutral wind, and the electrical conductivity of the E region at sunset are key characteristics inhibiting the process of prereversal enhancement, of the equatorial ionosphere which is being illustrated in Figure 3.1. The eastward motion driven by thermospheric neutral winds at ionospheric altitudes causes only ions to drift upward due to perturbation hence generating charge separation in effect producing electric field, which is projected onto the E region through magnetic field lines with high electric conductivity shown in Figure 3.1. and thus considered as equipotential line (KELLEY, 1989). The E x B drift induced by this electrical field has the same direction as thermospheric winds. Also, the F-region is short-circuited by the E-region with high Pedersen conductivity before sunset and at night, the conductivity is reduced by the decrease in E-region electron density, creating a downward electrical field in the F region. At the boundary of daytime and nighttime conditions, the eastward electrical field is intensified immediately before the reversal of the electrical field drift.

Figure 3.1 - Evening enhancement of the equatorial ionospheric electrical field by the F-region dynamo.

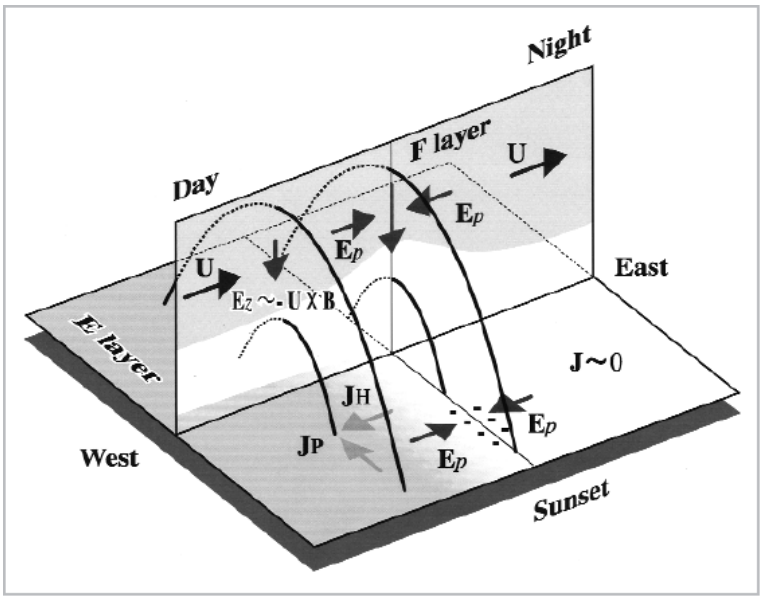

SOURCE: Farley et al. (1986).

3.2 The Rayleigh–Taylor instability

The collisional RT Instability is the primary destabilizing mechanism operating at the base of the F region followed by secondary instabilities. ESF is characterized by the presence of a wide spectrum of field-aligned irregularities. These instability mechanism can be explained by considering a sinusoidal perturbation in the ion and electron densities over the steady state value the F-region along the zonal direction. This plasma-depleted region is called a bubble.

Figure 3.2 - Initial F region plasma instability. Its evolution can lead to the Equatorial Spread F (ESF).

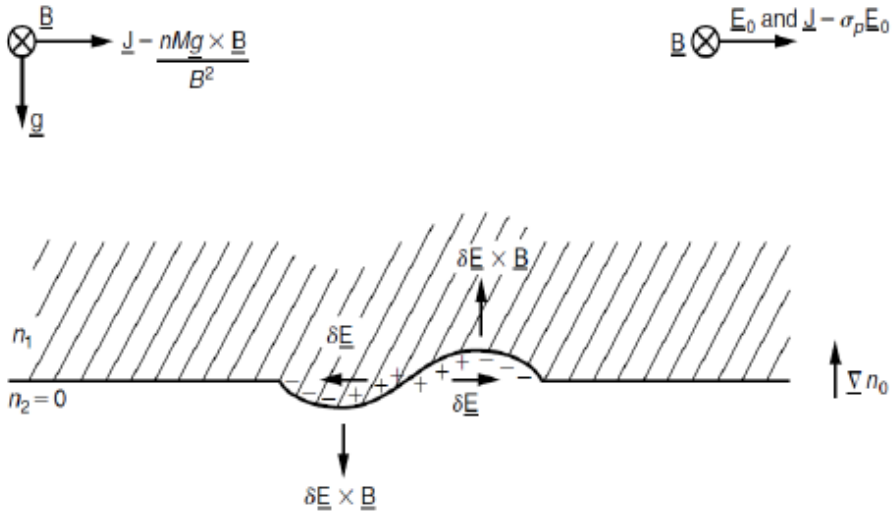

SOURCE: Kelley (2009).

The below equation expresses the growth rate (γ) of the instability:

$$\gamma = \frac{1}{L}[\frac{g}{v_{in}} + \frac{E}{B} + W_x(\frac{v_{in}}{\Omega_i}) - W_z] \tag{3.1}$$

where L is the plasma scale length, B is the geomagnetic field, g is the gravitational acceleration, v_{in} the ion-neutral collision frequency, E is the zonal electric field in the F-region, Ω_i is the ion gyro-frequency, W_x, W_z are the zonal and vertical winds respectively. It is now fairly well established that in the presence of an initial perturbation, the vertical electron density gradient through its plasma scale length L, and the base height of the F-region (essentially through the ion neutral collision frequency v_{in} are extremely important for the instability to get triggered. The growth rate of the primary Rayleigh-Taylor instability is inversely proportional to both L and v_{in} (SEKAR; RAGHAVARAO, 1987). In addition to these two, the neutral wind components (both vertical and zonal) also have a control on the growth rate, in the presence of an opposing gradient thus enhancing the growth rate (KELLEY, 1989). On the other hand, a poleward meridional wind, (diverging with respect to the dip equator) would stabilize the ionosphere by pushing additional ionization down to the E-region along the geomagnetic field lines. The third component, namely the

vertical wind would have a direct effect on the growth rate, similar to that of gravity, by physically separating the ions and electrons and by generating a polarization field (RAGHAVARAO et al., 1987). All these factors, more or less independent of each other, display significant variability on the occurrence.

Rayleigh-Taylor instability successfully explains many features of spread-F, This instability mechanism causes the onset and growth of plasma density irregularities in the ionosphere. The generation is discussed below.

Figure 3.3 - The eastward electric current generated by the difference in gravitational forces acting upon electrons and ions.

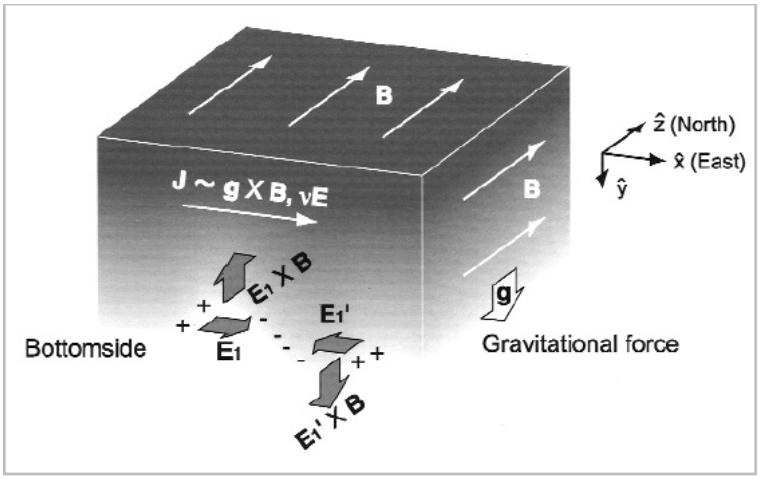

SOURCE: Farley et al. (1986).

Assuming that the ionosphere is perturbed by producing a small density fluctuation at the bottom side, causing a swing of isodensity surface in the region and hence becomes separated (electric current, electron, and ion) due to the transport system resulting in local positive or negative charge build up. These localized polarization electric fields have eastward and westward orientations regions, upward and downward so as for $E \times B$ drift in low-density and high-density respectively. As a result, density fluctuation is amplified, hence terming the condition as plasma instability. The equation 3.2 expresses the growth rate (γ) of the instability in a linear regime even though the derivation will be omitted [for more details see Sekar e Raghavarao (1987)].

$$\gamma = -\frac{g}{V_{in}}\frac{1}{n_{io}}(\frac{\delta n_{io}}{\delta_z}) \tag{3.2}$$

where g is gravitational acceleration, V_{in} the ion-neutral collision frequency, and n_{io} is the background electron density. The equation defined that the gravitational force and the electron density gradient are anti-parallel and that its magnitude is proportional to the density gradient. The density gradient on the very bottom of the F region rapidly steepens due to recombination at the bottom-side region after the ionization reaction ceases at sunset. The ionosphere becomes more unstable when the layer is high as the ion-neutral collision frequency decreases with altitude since the gravitational effects containing the ion-neutral collision frequency are determined by the vertical profile of the neutral atmosphere. The plasma bubble is thus essentially a nighttime phenomenon. During nighttime the electric field is on average westward (ABDU et al., 1985), contributing to a negative or low growth rate. i.e. a stable F layer bottom side. The density gradient reverses the F region peak. Furthermore, instabilities also develop similarly for electric currents generated by other causes. The Pedersen current due to the eastward electrical field generated by the dynamo effect and the effect of the collision between the neutral particles and ions in the downward neutral winds can both be treated similarly mathematically. The instability growth rate including the Pedersen current is given by the following equation:

$$\gamma = -(\frac{E}{B} + \frac{g}{V_{in}})\frac{1}{n_{io}}\frac{\delta n_{io}}{\delta_z} \tag{3.3}$$

where E, B are eastward electric field and magnetic field respectively. The additional term for the Pedersen current results in a positive growth rate when the electrical field is eastward. At the same time, the $E \times B$ drift by this electrical field pushes the region upward. i.e, the eastward electrical field contributes to the acceleration of instability growth, not only through the Pedersen current term but also by amplifying the gravitational term by upwelling in the region. This effect is most pronounced immediately after sunset when the eastward electric field is strengthened (evening enhancement). However, the term $\frac{g}{V_{in}}$ is larger during nighttime than daytime and increases due to the following conditions:

(i) V_{in} is proportional to the neutral density, n_o, where n is smaller during the night than the day; (ii) V_{in} is smaller at higher altitudes owing to the decrease in n_o with the altitude; and (iii) V_{in} is minimal during low solar activity. Recent studies using an ionosonde near the magnetic equator indicated that both post-midnight

field-align irregularities (FAIs) and uplift of the F layer frequently occur around midnight between May and August and again reveals that post-sunset enhancements are caused by pre-reversal enhancement of the zonal electric fields Abdu et al. (2003)

Also, the study estimated the linear growth rate of the Rayleigh–Taylor instability and proves that the uplift of the F layer could be enhanced the growth rate due to the increase in $\frac{E}{B} + \frac{g}{V_{in}}$.

During the night, the $E \times B$ drift velocity is downward, but the seasonal average of $E \times B$ drift velocity (E/B) is approximately 10 m/s for solar minimum conditions. The $\frac{g}{V_{in}}$ in remunerating for the negative value of E $\times$ B drift velocity, and thus the growth rate or the Rayleigh–Taylor instability becomes positive. This effect is most pronounced immediately after sunset, when the eastward electric field is strengthened (evening enhancement).

3.3 Seeding of medium-scale traveling ionospheric disturbances (MSTIDs)

The impact of atmospheric waves on ionospheric plasma and variability has been realized for a decade and more recent studies have indicated that the MSTIDs contribute to the generation of spread-F in equatorial and low-latitude regions of the earth ionosphere. These waves (such as gravity waves, planetary waves, tidal waves, and acoustic waves) are capable of transferring energy and momentum from one point to another as well as modifying the local thermodynamic state of the atmosphere (FRITTS et al., 2008).

Gravity waves are irregular motions in the thermosphere and ionosphere as proposed by (HINES, 1960). The irregular motions are termed Traveling Ionospheric Disturbances (TIDs), observed as the fluctuations in electron density in the ionosphere. Geomagnetic storms can also affect the motion of the neutral atmosphere traced by the modulation of the background ionization through the traveling ionospheric disturbances (TIDs). Traveling ionospheric disturbances are essentially the manifestation of atmospheric gravity waves (GWs) in the ionosphere. According to their different wavelengths (scales), there is a classification of three different types of TIDs LEITINGER (2005): 1. Large-scale TIDs (LSTIDs) with their origin in the auroral zone, with horizontal wavelengths greater than 1000 km, periods ranging from 30 min to 3 h and horizontal phase velocities of 300–1000 m/s. 2. Medium-scale TIDs (MSTIDs) with origins mostly in the lower atmosphere and also in the auroral zone. Horizontal wavelengths from 100 to 300 km, periods from about 12 min to 1 h and

horizontal phase velocities from 100 to 300 m/s. 3. Small-scale TIDs (SSTIDs) with origins only in the lower atmosphere. The corresponding wavelengths, velocities, and periods are smaller than those of MSTIDs because they belong to the acoustic branch.

Fukushima et al. (2012); indicated that nighttime MSTIDs could be classified into two groups. The first group has their origin in GWs which are possibly generated from deep convection. Abdu et al. (2009); presented a study which compared the observational results with the theoretical model calculation results and provided the evidence that the GWs could seed ESF, which agreed well with the results shown by (KRALL et al., 2013). It is known that TIDs are a manifestation of GWs in ionosphere (HINES, 1960) and MSTIDs/GWs could be supposed to be seeding of spread-F.(LAN et al., 2019); showed that wave-like structure in the ionosphere, induced by MSTIDs/GWs, also could produce spread-F on ionograms. The second group of nighttime MSTID is related to plasma density irregularities developed at mid-latitudes. Candido et al. (2011); proposed that low-latitude spread-F, SF could be caused by nighttime MSTIDs. (PIMENTA et al., 2008) presented that nighttime MSTIDs generated in the mid-latitude region could propagate toward the low-latitude region and generate nighttime SF from all-sky imaging system observation.

MSTIDs propagation direction depends on the time of the day, season as well as the latitudes and the hemisphere of the source region. The daytime MSTIDs occur in winter and tend to propagate southeastward and northeastward in the northern and southern hemispheres respectively ((TSUGAWA et al., 2007); (OTSUKA et al., 2013). The nighttime MSTIDs occur during the summer months and propagate southwestward in the northern hemisphere (OTSUKA et al., 2013) in the southern hemisphere and (PIMENTA et al., 2008). The dawn and dusk MSTIDs occur frequently in summer and propagate eastward and north-northwestward respectively Otsuka et al. (2011). Besides, the concept of gravity waves is important to the dynamic processes that occurs in the atmosphere/ionosphere leading to MSTIDs.

3.4 Seeding of atmospheric gravity waves

An atmospheric gravity wave is an oscillation of neutral air that causes ion-neutral collisions and eventually generates a polarization electric field in the F region. The atmospheric gravity wave propagates at the thermospheric and F-region heights. In addition to these, those originating from tropospheric convective sources dissipate energy and momentum at E and F region height. These gravity waves could affect structure and the dynamics of the F-region.

Gravity waves can seed the instability by providing perturbations in the bottom side electron density in which the polarization electric field grows in a way to enhance additional growth of density depletion due to the intensification caused by the polarization electric field and hence yielding the instability growth process by aligning along the dip equator. (TSUNODA, 2010) has compared tropospheric convection activity with the occurrence of equatorial spread F (ESF), and showed that the occurrence rate of the ESF is highest when the active convection region is located near to the magnetic dip equator. The result obtained indicated that atmospheric gravity waves launched from the active convection region in the troposphere could propagate into the thermosphere and contribute to plasma bubble seeding.

The bottom side density gradient region becomes unstable to general Rayleigh-Taylor instability thereby increasing the instability growth rate due to the rises caused by these gravity waves. (HUANG; KELLEY, 1996); showed that the polarization electric fields induced by the neutral wind oscillations due to gravity waves can initiate the Rayleigh– Taylor instability and that the special resonance of the gravity waves and the plasma motion can speed up plasma bubble formation.

Furthermore, the gravity waves cause a huge increase or decrease of PRE amplitude depending upon the gravity wave phase when the zonal winds are perturbed which might favor or decrease the instability growth rate through $(\frac{E_o X}{B_o}/l_o)$ where $l_o)$ is electron density gradient scale length and affect the gravitational RTI growth rate factor $(\frac{g}{V_i}/l_o)$. In conclusion, other research work also suggested that gravity waves might be related to the development of large-scale wave structures.

3.5 Literature review of Equatorial spread-F

Equatorial spread-F is a spectacular phenomenon in which the equatorial region ionosphere is reshaped after sunset. Spread F or Equatorial Plasma Bubbles (EPBs) can be associated with ionospheric scintillations which can influence the performance and reliability of space-borne and ground-based electronic systems that may cause the disruption of satellite operations, communications, navigation, and electrical power distribution grids, leading to potentially broad economic losses. The others effects are due to Space Weather events.

3.5.1 The physical picture of ESF

After the sunset, the E-region begins to recombine, and there is effectively no E-region conductivity to short out any irregularities in the F-region. Due to the chem-

ical processes and electrodynamic effects, a steep upward-directed electron density gradient develops at the bottom side of the F-region. Plasma density fluctuations will grow on the bottom side via a collisional RT instability mechanism (KELLEY, 2009). The collisional RT instability generated irregularities and bubbles developed in the bottom side F region rise beyond the F region peak by polarization ExB motion through the F-peak and cause topside spread-F. The ESF irregularities occur over a wide range of scale sizes from a few tens of kilometers to a few Centimeter.

The Equatorial spread-F (ESF) is studied by using several instruments, including ground-based radar, sounding rockets, conventional ionosondes, topside ionosondes, in situ probes, airglow measurements, and propagation of satellite beacons (phase and amplitude scintillation). Spread F has been widely studied since it was first defined on the ionogram in the early 1930s. Several observations since then revealed the main morphological features of spread-F occurrence, including its dependences on solar and magnetic activities, season, longitude, latitude, local time, and the background ionosphere. Early investigations of the ionosphere observed diffuse echoes in data from measurements using ionosondes, which are high-frequency radars used for ionospheric sounding (ABDU et al., 1981).

Spread-F signatures recorded by the ionosonde were classified into four types: frequency spread-F (FSF), mixed spread-F (MSF), and range spread-F (RSF) according to the description given by Abdu et al. (1985) in their URSI Handbook of Ionogram Interpretation and Reduction, and strong range spread-F (SSF) defined according to Piggott e Rawer (1972). The term spread echo is applied to the condition observed at middle and low latitudes, and quite often in polar regions. when the ionospheric echo becomes quite diffuse, loses its sharply defined structure, and extends to frequencies sometimes far above those indicative of the actual ion density of the layer. When it occurs in F region echoes, this condition is called spread-F.

The gravitational Rayleigh–Taylor instability (R–T) theory was the primary mechanism to explain the formation of irregularities in the equatorial region. Spread-F occurrences at mid latitudes are affected by many factors (Kelley (1989), Abdu et al. (1998)). Other factors are MSTIDs and gravity waves. Gravity waves were considered to be a seeding mechanism that creates density perturbations in the ionosphere, leading to spread-F at mid-latitude regions. Since most of the gravity waves in the ionosphere originate from the lower atmosphere, there should be some regional features of spread-F occurrences due to the different local meteorological or ground conditions.

Furthermore, Bertoni et al. (2011), present a study on the ionospheric Equatorial spread-F (ESF) occurrence and morphologic features, based on measurements made during the period of October 2005 and January 2006 and May– July 2006 by digital ionosondes operating at two near magnetic equator locations and stated that Pre-midnight RSF is the most common type observed at Palmas and Manaus. The term "spread F" is widely known to be irregularities observed in equatorial and low-latitude regions. Nowadays digital ionosondes are extensively used for ground-based sounding of the ionosphere providing information from the E region to the peak of the F layer, over a variable range of frequencies as well as features related to the propagation of the irregularities (ABDU et al., 1998).

The instabilities present in the equatorial ionosphere after sunset are known to generate large-scale depletions in the ambient electron density and are commonly referred to as Equatorial Plasma Bubbles (DASHORA; PANDEY, 2005) which rise vertically and then drift for several hours. Spread-F or Equatorial Plasma Bubbles (EPBs) can be associated with ionospheric scintillations which disrupt or cause errors in navigation and positioning systems. The interference and the interruptions to space-based application systems posed by these structures highlight the need to predict their occurrences in space and time, which demands a detailed understanding of the mechanisms of their generations. However, recent observations during a solar minimum period show a high occurrence rate of irregularities post-midnight around the June solstice. Several seeding mechanisms have been proposed for ESF onset: GRT, MSTIDs and gravity waves, etc see, for instance (ABDU et al., 1998). The mechanisms for generating the post-midnight irregularities as been stated by Otsuka (2018) but the generalized Rayleigh-Taylor (GRT) instability is widely accepted as the mechanism which generates the post-sunset equatorial spread F (ESF). The vertical plasma drift is one of the main drivers of the GRT instability, and the pre-reversal enhancement (PRE) of the drifts near sunset can explain most of the climatological features in ESF including its high occurrence rate in the evening sector. Gravity waves are generally taken as a seed for the GRT instability initiation. On the other hand, the Post-Midnight Spread F (PMSF) events, continue to have a controversy on its Physical mechanism, which generates them. The source of the eastward electric field necessary to elevate the F-layer and generate the instability was attributed to disturbance dynamo which occurred even during very moderate auroral activity. Many of the observed PMSF are attributed to fossil ESF events which were generated westward of the observing location, drifted eastward, and reached the observing site after midnight. In addition, the uplift of the F layer by the meridional neutral winds in the thermosphere which may be associated with

midnight temperature maximums in the thermosphere Abdu (1997). Ionospheric irregularities can occur in equatorial plasma bubbles. Plasma bubbles are well-known to frequently occur post-sunset when the solar terminator is nearly parallel to the geomagnetic field lines (during equinoxes at the longitude where the declination of the geomagnetic field is almost equal to zero and near the December solstice at the longitude where the declination is tilted westward), especially during high solar activity conditions via the Rayleigh–Taylor instability.

Figure 3.4 shows range-time intensity (RTI) plots of VHF radar backscatter power for two nights during the second SpreadFEx measurement interval, 24/25 and 25/26 October 2005.

Figure 3.4 - Spread F and plasma bubbles observed in the zenith on 24/25 (top) and 25/26 October 2005 (bottom) by the VHF radar at Sao Luis during the SpreadFEx measurement campaign.

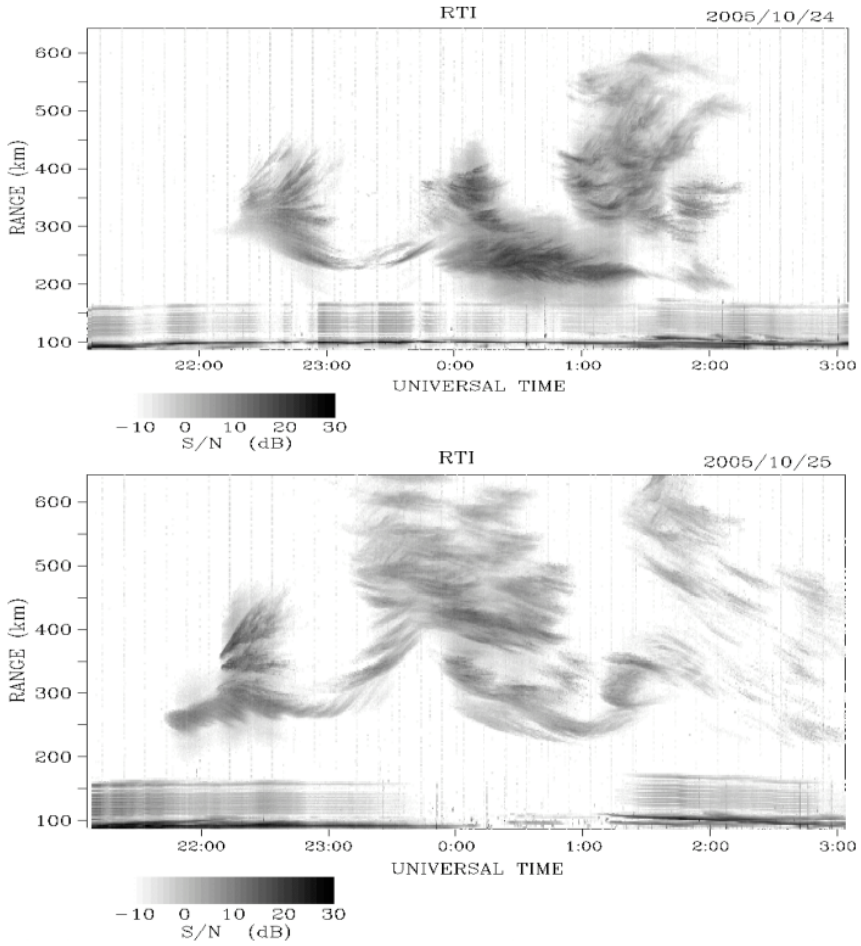

SOURCE: fritts (2009).

Figure3.4 shows plasma bubbles apparently initiated near 250 km and extending to over 600 km with a temporal spacing between 1 and 2 h. Significantly, these responses at the bottomside F-layer coincide with the presence of deep convection 800 km south and northwest of Sao Luis.

Figure3.5 shows two sets of airglow depletion images, one for 0300 UT/2320 LT and another for 0330 UT/2350 LT, together with the corresponding ionogram Spread F manifestations over the two stations.

Figure 3.5 - Ionogram over Boa vista and Campo Grande using all-sky images in the nighttime of 9/10/2002.

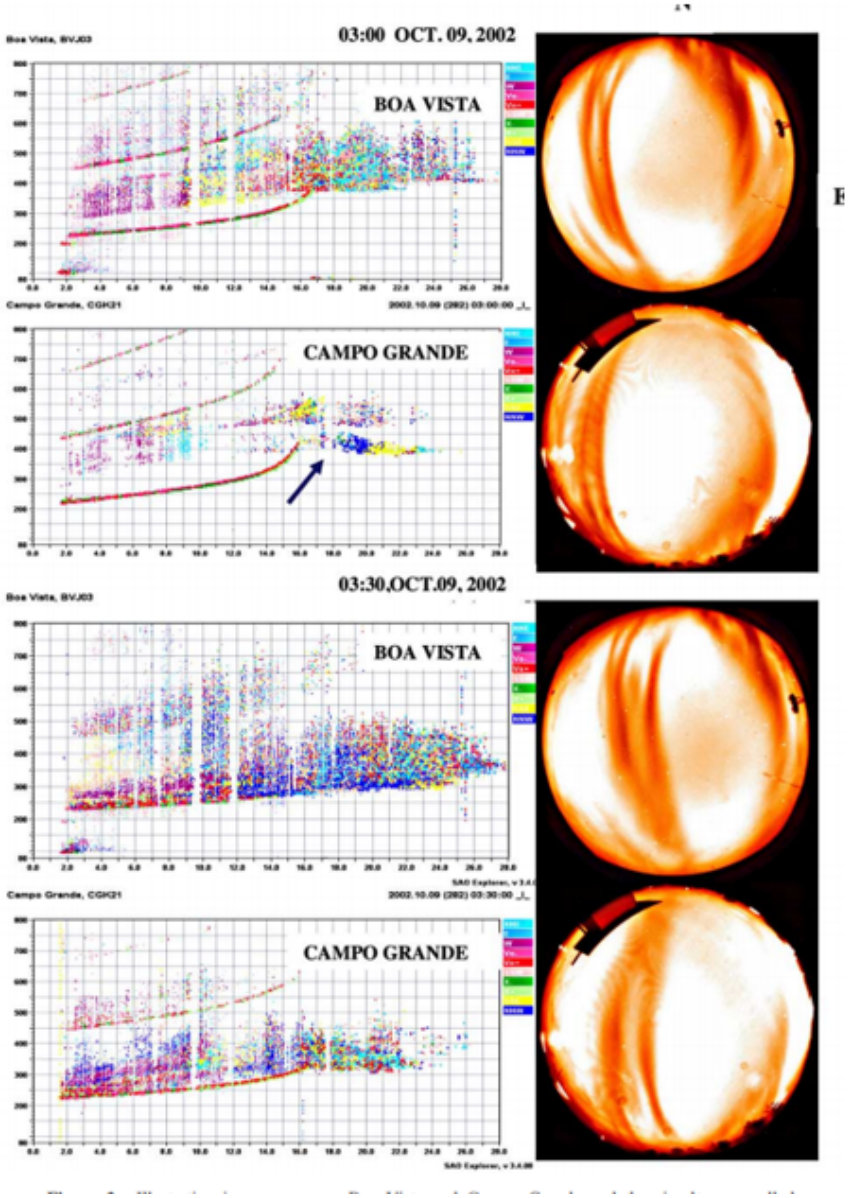

SOURCE: Abdu et al. (2009).

In figure 3.5 bubble structures appear to have developed westward, probably initiated by a vertical drift increase in the preceding hours (near 0100 UT) Abdu et al. (2009).

Figure 3.6 shows ionograms of range type at Okinawa and Yamagawa (low latitudes) and frequency type at Kokubunji and Wakanai (mid- latitudes) in japan.

Figure 3.6 - Sample ionograms of spread-F at Mid-latitude in japan.

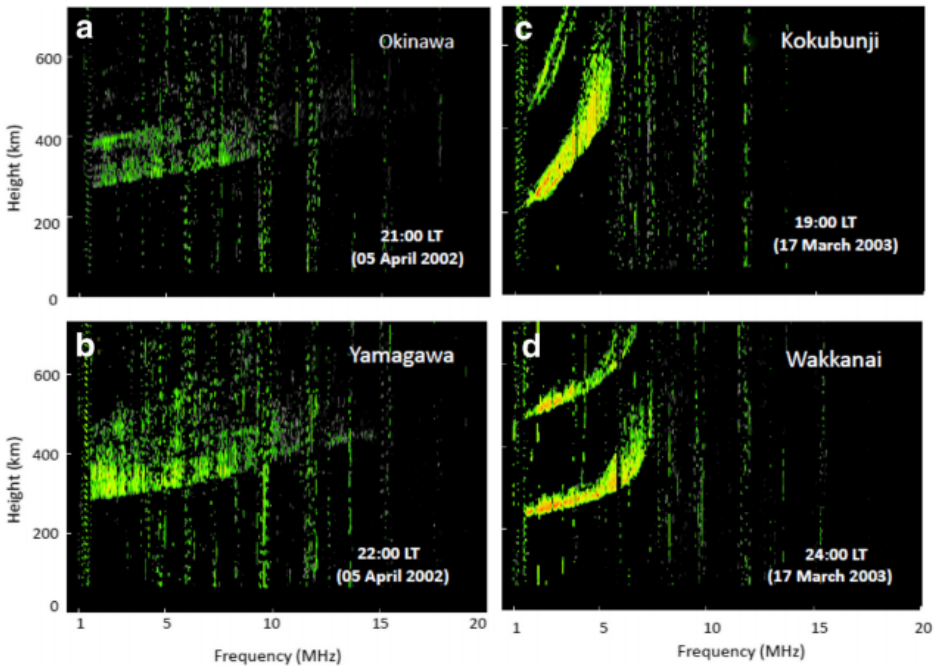

SOURCE: Balan et al. (2018).

Figure 3.6 shows spread-F at Okinawa and Yamagawa is range type and that at Kokubunji and Wakanai is frequency type. The spread-F in these stations are found to be of the same type at all levels of solar activity except for a few cases which are not distinguished in the analysis. The spread-F in these stations are found to be of the same type at all levels of solar activity Balan et al. (2018).

Figure 3.7 shows the statistics of the post-midnight spread F for June months over Jicamarca.

Figure 3.7 - The statistics of Spread F occurrence for June months during solar cycle 23-24 over Jicamarca during 2001–2009.

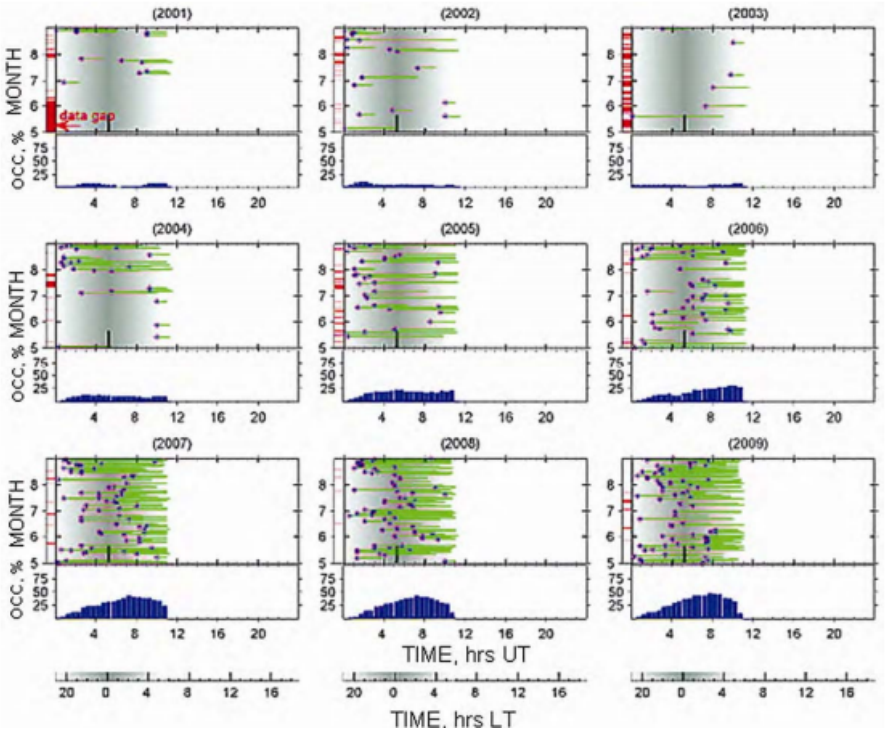

SOURCE: Li et al. (2011).

Figure 3.7 occurrence rate peaks near 0300 hrs LT (0800 hrs UT) and it increases from near 0% in solar maximum (2001) to about 50% in solar minimum (2009) as shown in Figure 3.7. This indicates that the solar activity trend in the occurrence rate of the post-midnight irregularities in June solstice months is similar in the entire South American sector Li et al. (2011).

Figure 3.8 shows a sequence of ionograms on 25–26 July 2011 from 00:40 to 03:10 LT over SL (top panel) and over the FZ low-latitude site (bottom panel); from 25 July 2011 at 22:00 LT to 26 July 2011 01:30 LT, the presence of unusual spread F patterns is observed.

Figure 3.8 - Sequence of ionograms obtained from São Luis (SL) and Fortaleza (FZ) of Brazil, showing the unusual pattern of spread-F in June Solstice 2011.

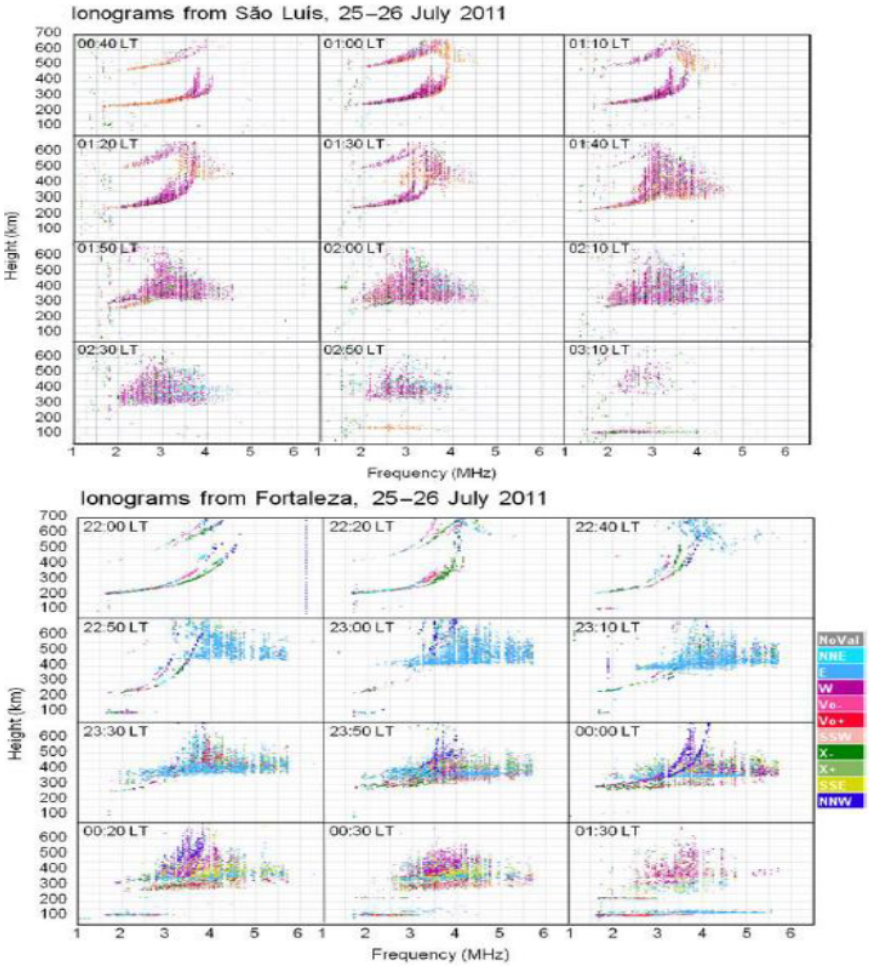

SOURCE: Candido (2019).

In figure 3.8 shows a sequence of ionograms on 25–26 July 2011 from 00:40 to 03:10 LT over SL (top panel) and over the FZ low-latitude site (bottom panel); from 25 July 2011 at 22:00 LT to 26 July 2011 01:30 LT, the presence of unusual spread-F patterns are observed. Over SL, the first spread-F trace appears at 01:00 LT at an oblique angle close to or above the F-layer peak at a virtual range of 600 km. Candido (2019).

The Range type spread-F

Range spread-F ionogram traces represent irregularities located mainly at the F

region. The range type spread-F is when the diffuseness is principally along the horizontal part of the trace giving rise to ambiguity in height but the critical frequency is identifiable. The range type of spread-F, often associated with the occurrence of medium- and large-scale irregularities, including EPBs. It is comprised of trace patterns with the echoes spread-F in range, and with the onset beginning at the lower frequency end of the F-layer trace in ionograms. Traces are normally away from the critical frequency, showing broadening in range and are capable of exceeding 30 km in virtual height. The type of pattern produced depends on whether the difference in electron density in the field-aligned structures is large or small compared with the ambient electron density. When intense, RSF transforms into strong-range spread-F (SSF) in which the ionogram traces are characterized by an extended range spread-F echo that significantly extends well past the critical frequency of the F region (foF2), covering the whole ionosonde frequency range.

Figure 3.9 - Representation of Range spread-F on ionogram in Belem 2018.

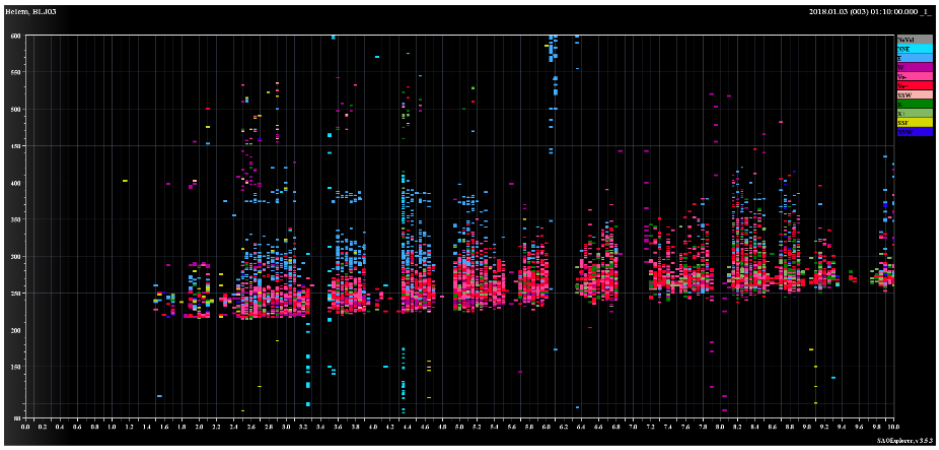

The Frequency type spread-F

Frequency spread-F ionogram traces represent irregularities located near the F region peak. The Frequency type spread-F is when the spreading is maximum at frequencies close to the penetration frequencies causing ambiguity regarding the identification after foF2. It is believed to be associated with smaller-scale decaying irregularities following spread-F EPBs (ABDU et al., 1981). Some studies have

pointed out that frequency-type spread F can sometimes be associated with patches of ionization propagating eastward.

The frequency spread F (FSF), which shows a spread near the critical frequency, as if traces were displaced in frequency but are still present at the same time. The traces near the critical frequencies are broadened and may show additional traces similar to a normal critical frequency trace. FSF is the most common type of spread-F at most latitudes and the spread is normally greater than 0.3MHz.

Figure 3.10 - Representation of Frequency spread-F on ionogram in Belem 2018.

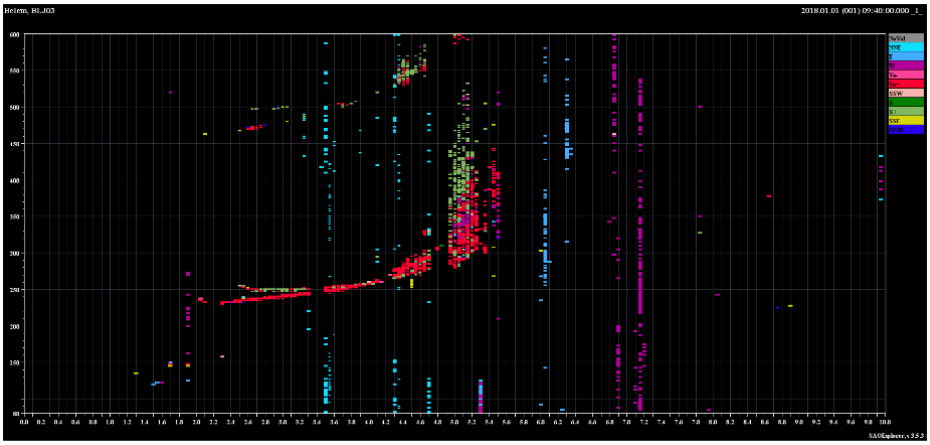

The Mixed spread-F

Mixed spread-F ionogram traces represent irregularities located throughout the F region. On some occasions spreading is seen to be equally prominent in the height scale in the entire range of observed ionogram and is classed as complete spreading. Also when both frequency and range spread-F types can appear simultaneously. The traces are broadened in both range and frequency but not show the presence of either type distinctively.

Figure 3.11 - Shows the representation of Mixed spread-F on ionogram in Belem 2018.

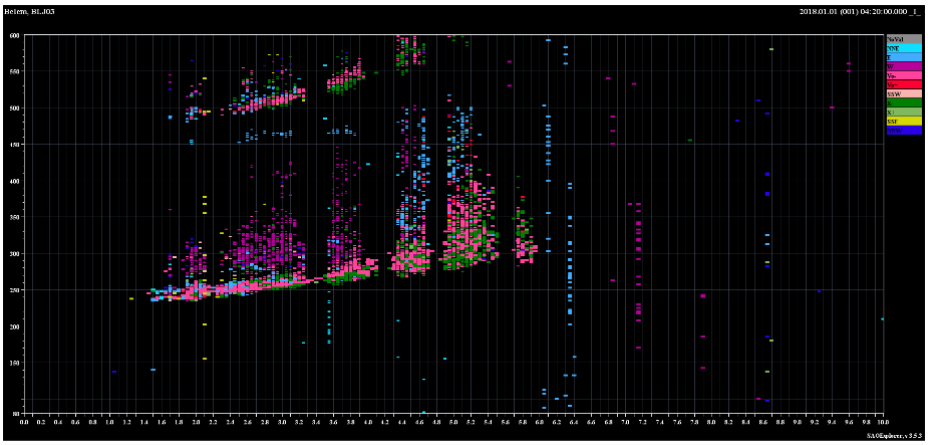

3.6 International Reference Ionosphere - IRI Model -2012

According to Bilitza (2018), International Reference Ionosphere (IRI) is the international standard for Earth's ionosphere and is recognized as such by COSPAR and URSI and most importantly by the Organization in charge of international standards the International Standardization Organization (ISO). IRI provides monthly averages of the electron density, electron temperature, ion temperature, and ion composition in the ionospheric altitude range. There are a number of different ways in which measurements are being used to drive IRI towards describing conditions as realistically as possible: (1) solar, magnetic, and ionospheric indices that are deduced from solar, magnetic, and ionospheric measurements; (2) equivalent solar or ionospheric indices obtained by adjusting the model to ionospheric measurements; (3) direct updates locally if measurements of characteristic parameters are available; (4) assimilation of available data into the IRI background model (for more details see `https://ccmc.gsfc.nasa.gov/modelweb/models/iri2012_vitmo.php`).

Figure 3.12 - Interface of IRI parameters varying with height, latitude, longitude, year, month, day of month, day of year, and hour of day.

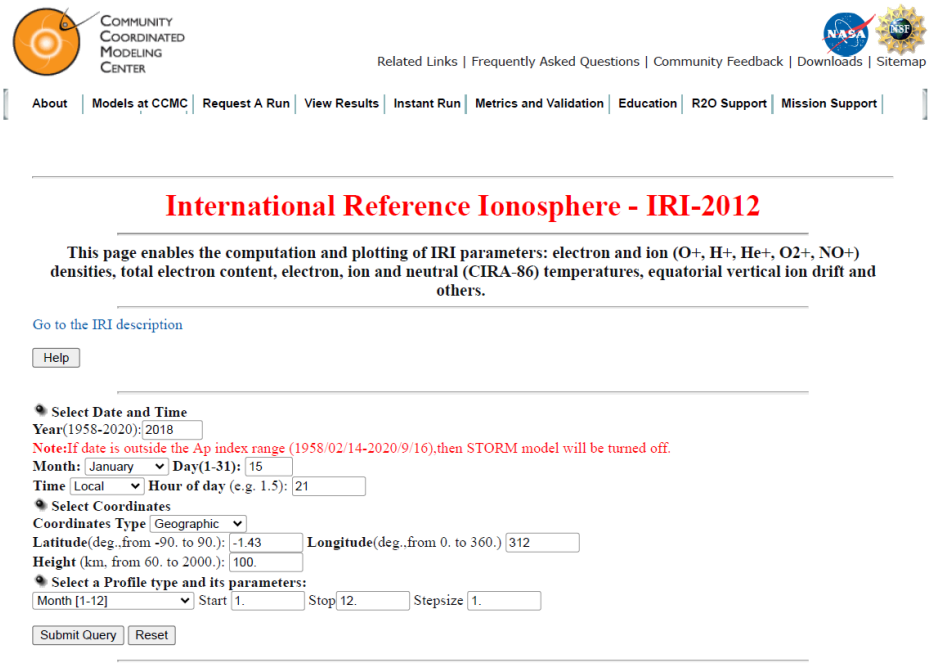

The statistics of equatorial spread F Probability was compared with International Reference Ionosphere model, IRI to find the percentage probability rate or otherwise if there is a correlation. The spread-F probability model was implemented by Abdu et al. (2003) based on ionosonde measurements from the Brazilian longitude sector. Furthermore, a well-developed ESF event is marked by spread F in ionograms in a wide range of latitudes extending from the magnetic equator to around $\pm$ 25° in magnetic latitude. On the other hand, a weak event can be said to be characterized by the occurrence of ionogram spread F traces restricted to the immediate vicinity of the magnetic equator which may be termed just as an equatorial bottom-side spread F event. Thus an empirical model(IRI model) of the statistics of spread F distribution versus latitude can be considered to be equivalent to the statistics of the equatorial bottomside spread F or those of the plasma bubbles depending upon the latitudinal separation of the station from the magnetic equator, as stated by Abdu et al. (2003).

3.7 High-speed solar-wind streams, Corotating Interaction region and geospace interactions

High-speed solar-wind streams emanate from solar coronal holes; the fast wind interacts with upstream slow streams producing regions of enhanced magnetic field strength and particle density that are known as co-rotating interaction regions. Due to the recurring nature of coronal holes near the solar minimum, this results in periodic driving of the magnetosphere that can last for several days and input as much energy as a storm driven by a coronal mass ejection. CIRs and HSSs are important drivers of geomagnetic activity, though they are not usually associated with large geomagnetic storms which are usually CME-driven. Storm strength is traditionally judged from the DST index, which is a measure of the magnetospheric ring current derived from near-equatorial ground magnetometer measurements. During large geomagnetic storms, the DST has a minimum of less than –100 nT; such storms also have a strong solar-cycle dependence, peaking at solar maximum because they are driven by CMEs, which occur more often on an active Sun. Weak storms (–75 < DST < –35 nT) have a much smaller solar cycle dependence, being more common in the declining phase of the solar cycle (e.g Gonzalez et al. (1994)). Although CIRs do not produce strong ring currents, they do drive storm levels of other phenomena such as enhanced convection, precipitation and relativistic electron energization. The reason for the difference during CIR and CME storms is likely to arise from the nature of the IMF; during CMEs there is usually a large, persistent southward turning of the IMF (negative BZ), accompanied by high solar-wind speed. This enhances magnetic reconnection on the dayside, which adds open magnetic flux into the Earth's magnetotail and transfers energy into the system. This energy is released via explosive reconnection events in the tail known as substorms (e.g. Akasofu (1964)), which inject energetic particles into the inner magnetosphere and cause the precipitation that produces dynamic auroral displays.

4 INSTRUMENTATION AND METHODOLOGY

Comprehensive experimental and theoretical research has been done in the last 30 years to study equatorial spread-F. These studies have shown that plasma instabilities play a major role in the generation of the irregularities. The purpose of this chapter is to present the instrumentation and the methodology used in this thesis.

4.1 Digisonde and its operation

The ionosonde is an ionospheric sounding instrument, which works from a transmitter/receiver system, emitting sequential pulses of electromagnetic energy at frequencies ranging from 0.5 to 30 MHZ (REINISCH et al., 2005). The ionosonde manufactured by Lowell Digisonde International is called Digisonde and stands for Digital Ionospheric Goniometric IonoSONDE. Digisonde data was used in this work.

The equipment is designed to directly measure the transit time, t, that a pulse of radio waves takes to propagate at the transmitter-ionosphere-receiver interface, depending on the frequency, it enables the understanding of the behavior of radio waves when propagating through the ionosphere, providing information necessary to understand the factors that directly influence ionospheric phenomena. The radiofrequency signals transmitted by the Digisonde will be reflected in the ionosphere when the pulse frequency is equal to the natural resonance frequency of the ionospheric plasma (REINISCH, 1983), "thus the receiver, having its transit time recorded and the distance between ionosphere and Earth's surface is calculated." The pulses are transmitted with peak power in the order of 10 kW for the DGS 256 Digisonde models and of the order of 300 W for the Digisonde Portable Sounder (DPS) (REINISCH; XUEQIN, 1982). The spacing of the receiving antennas forms an equilateral triangle 60 m long at the base, with one of the antennas located in the center of the triangle as shown in Figure 4.1.

Figure 4.1 - Configuration of the Digisonde's antenna array receiving.

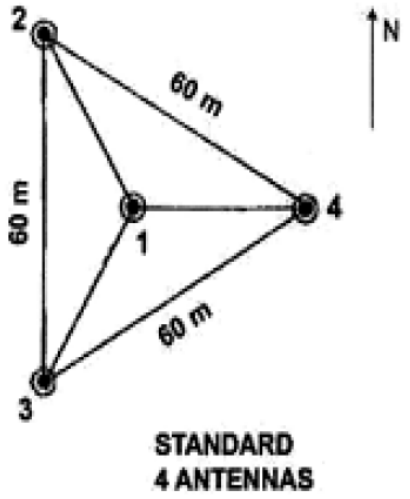

From time elapsed (t) between a transmitted pulse and its reception after being reflected by the ionosphere, the virtual height of the ionospheric layer h^I (DAVIES, 1965) can be calculated according to the expression:

$$h^I = \frac{1}{2}ct \tag{4.1}$$

where c represents the speed of the electromagnetic wave in a vacuum. Such as pulse speed is less than the speed of light and varies with electronic density of the propagation medium, the actual height at which the reflection actually happened is always less than the "virtual height (h^I)".

This occurs because there is a delay of the electromagnetic signal due to the ionization below the reflection point. The basic principle of operation of the digisonde consists of the reflection and refraction of electromagnetic waves by ionospheric plasma. Neglecting effects of the geomagnetic field, as well as collisions between electrons and neutral particles, the ionospheric plasma refractive index μ is given by (RATCLIFFE et al., 1972).

$$\mu^2 = 1 - x = 1 - \left(\frac{F_N}{F}\right)^2 \tag{4.2}$$

Thus; reflection occurs when the plasma frequency of the ionosphere is equal to the transmitted frequency.

$$F_N{}^2 = F^2 \tag{4.3}$$

Due to the presence of the Earth's magnetic field,(i.e interaction between the plasma and Earth´s magnetic field) the ionosphere behaves as a birefringent medium imply that two reflected signals appear: the ordinary and extraordinary signal.

$$\mu^2 = 1 - \frac{X(1-X)}{1-X-Y^2} \tag{4.4}$$

F represents the frequency of the wave and is expressed as;

$$F_N{}^2 = \frac{N_e e^2}{4\pi^2 \varepsilon_\circ m} = F^2 \tag{4.5}$$

Where:
Ne is the electronic density;
m is the mass of the electron;
e is the charge of the electron;
$\varepsilon_\circ$ is the electrical permittivity in a vacuum;
Fn is the frequency of the plasma; and
F is the frequency of the electromagnetic wave.

In neutral atmosphere, X= 0. In the presence of free electrons, X tends to increase, and the refractive index starts to decrease gradually until the incident wave reflects through the middle, so: $\mu = 1$ is initially considered, because below the ionosphere Ne can be considered null.

For an extraordinary wave, the refractive index of the ionospheric plasma will be given given by the equation 4.4 with Y expressed by:

$$Y = \frac{eB}{2\pi m F} \tag{4.6}$$

The relationship between plasma frequency and wave frequency, expressed by equation 4.5 allows determining the electronic density of the ionospheric layer. Knowing

the values of the constants and the transmitted frequency, the electronic density profile is calculated.

The signal reflected echoes by the ionospheric layers are recorded using graphs, referred to as ionograms. Ionograms represent the virtual height of reflected echoes of the electromagnetic pulses transmitted by the Digisondes as a function of their frequencies Reinisch et al. (2005). Its measurements enable the vertical profile of electronic density, the plasma drift speed, and the polarization, among other information of the ionosphere to be studied.

4.2 Digisonde online databasing and quality control via SAO explore

The dependence on quality control and verification of the autoscaled data has emerged base the use of ionograms. This has resulted in high focus placed on development of techniques for automated quality control of autoscaling results Reinisch et al. (2005), it is critical for many research and applied projects to edit the derived ionospheric characteristics by human inspection. Therefore a good data management system is critical and important for accuracy in the ionogram-derived characteristics. There are three key elements of the digisonde data management system are: (1) the "SAO Explorer", a digisonde data visualization and editing tool, (2) "DIDBase" (Digital Ionogram Database) holding raw and derived digisonde data under an industrial-strength database management system, and (3) "ADRES" (Automated Data Request Execution System) capable of accepting the "ground truth" requests for particular periods of time and locations and actively managing the process of acquiring, verifying, and reporting the requested data. In this work SAO Explorere was observed to be more reliable and efficient as compareed to the others and capable of analyzing thousands of ionograms. SAO-Explorer is a digisonde data analysis tool used for manual verification and editing of autoscaled digisonde ionograms, as well as a variety of visual presentations of ionograms and derived ionospheric characteristics.It serves best for the in-depth study of particular periods of time or locations where background ionograms are required to aid with data interpretation. The SAO-X workstations are granted both read and write access to the DIDBase allowing full scale, platform-independent, concurrent, remote operations with the archived data over the Internet (REINISCH et al., 2005). Some examples of typical SAO explorer outputs are shown in Figure 4.2 `https://ulcar.uml.edu/Installation/SAO-X/install.htm`.

Figure 4.2 - Interface of ionograms Data processing using SAO explorer.

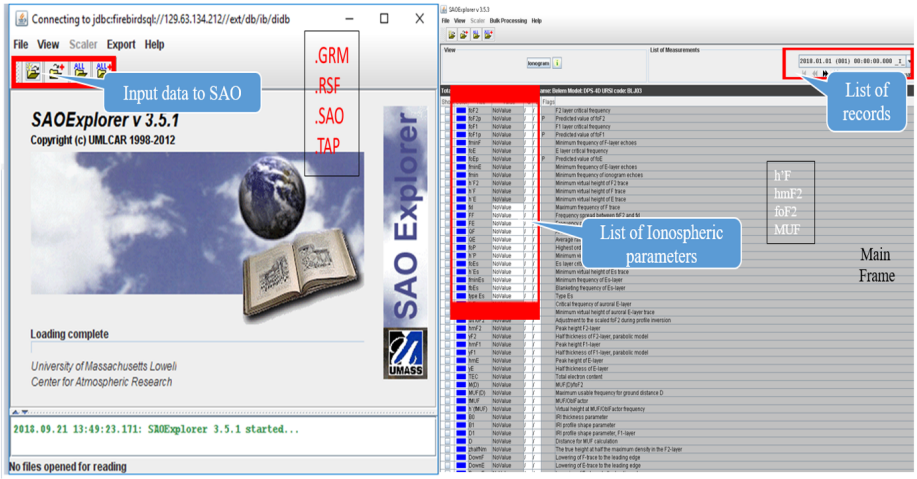

Figure 4.3 - Features of SAO explorer displayed on ionogram.

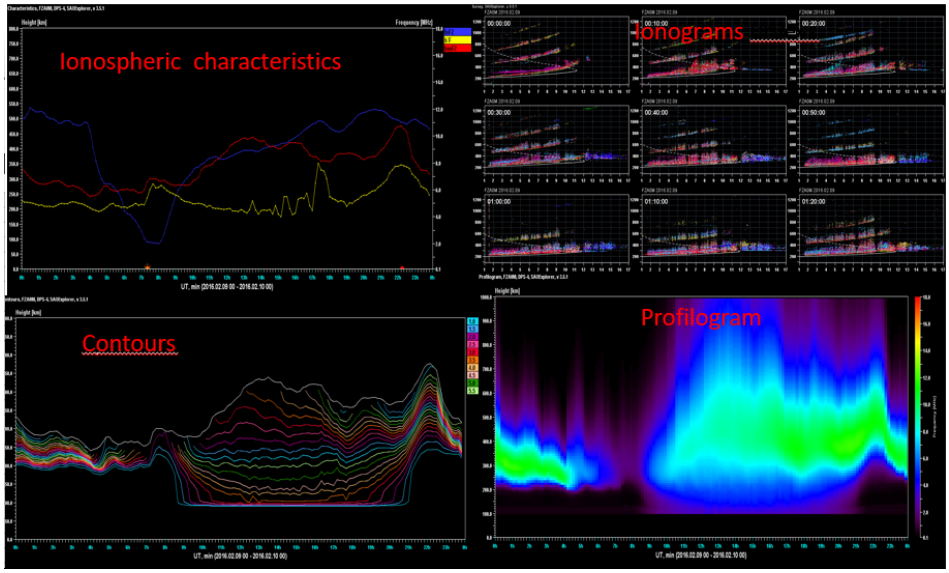

Figure 4.3 shows the various "Characteristics" of the ionospheric parameters such as (h'F, hmF2, foF2), of which base on ionogram survey would aid to identify the

factors affecting the electromagnetic waves. The “Profilogram” shows the vertical electron density distribution as Function of time Reinisch et al. (1994). The colors indicate the electron plasma frequency in MHz. The “Contour” plots displays the true height for the selected plasma frequencies as a function of time. The colors in ionograms code indicate wave polarization and echo arrival direction. The example shows equatorial data for Belem, Brazil.

Ionosondes, through their sounding techniques, provide direct and accurate measurements of the ionospheric plasma density and others parameters: F-layer heights, etc. Spread F signatures on ionograms provide information on the distribution of irregularities. Ionosondes directly measure electron density at the ionospheric F2 layer peak (NmF2) and they are usually used as diagnostic tools for calibrating other more complicated observation methods such as incoherent scatter radar, satellite beacon tomography and radio occultation Bertoni et al. (2011). The virtual height can be converted into time, assuming that the speed of the wave is equal to the speed of light. The signal amplitude is represented by the number of pixels on the curve. Doppler shift is related to the color of the curve and polarization is related to the color code.

Figure 4.4 - Ionogram taken from a Digisonde installed in Sao Luis, on Jan 29, 2003, at 11:00 UT (08:00 LT).

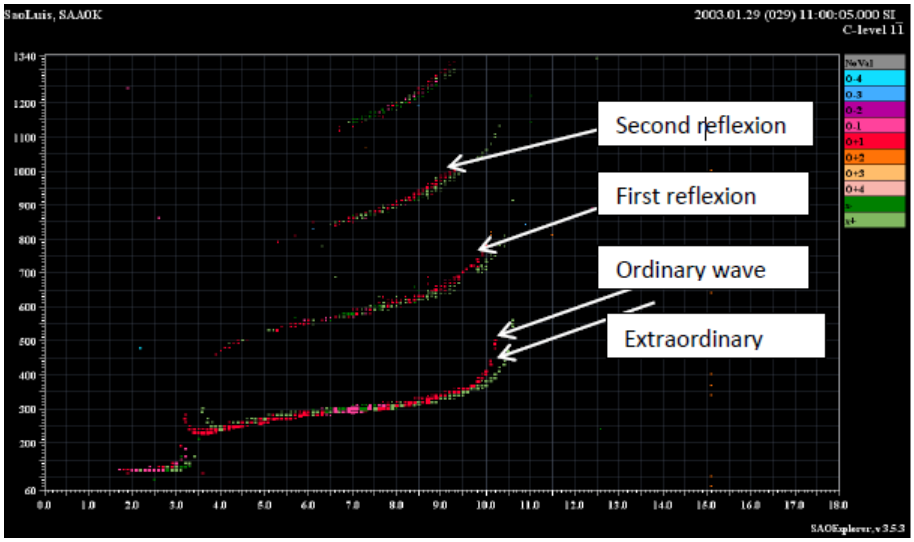

Figure 4.5 - Ionogram taken from a Digisonde installed in Sao Luis, on Jan 7 and 8, 2009; Top panel: Day time; Bottum panel: Night time.

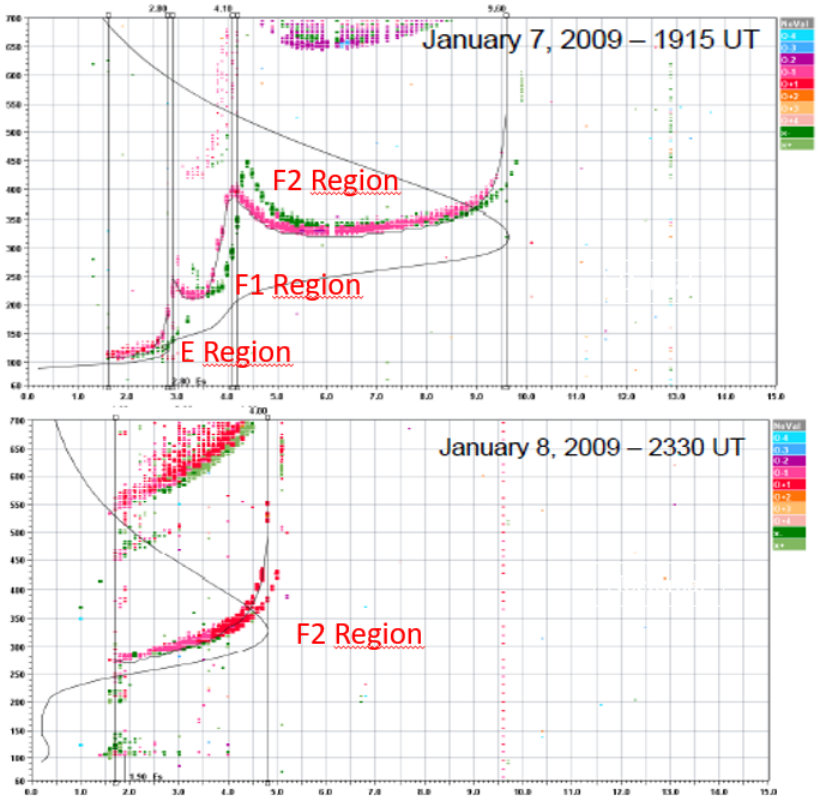

4.3 Method of analysis of the ionograms

The electromagnetic wave transmitted to the ionosphere is linearly polarized. In the presence of the Earth' magnetic field it splits in two waves circularly polarized: one to the right and the other to the left. These two waves travel at different velocities so they arrive to the receiver at the Earth at different times. This is why two different traces in the ionogram can be seen. In the example shown in Figure 4.4 the red trace is the signature of the ordinary wave and the green trace is due to the extraordinary wave. Sometimes extra traces appear in the ionogram in diferent altitudes as seen Figure 4.4. The multiple traces happens when the return signal is reflected by the Earth goes to ionosphere and come back, sometimes several times before it is attenuated. These multiple echoes appear on an ionogram at multiples of the original virtual height. ARTIST software performs the inversion of the ionogram to obtain the altitudinal profile N_e, meaning the dependence of N_e with the true

height Reinisch et al. (2005). The ionogram can be edited by manual scaling the data. The color code showing the direction of echoes that form the spread-F.

For the purpose of this study, it were analyzed ionograms taken from a Digisonde installed at the equatorial station, Belém,(BL; 48°W, 1.43°S; Dip: -2.6°), for the whole year 2018. The ionograms are recorded in a cadence of 10 minutes, as there are 144 ionogramas per day. It were manually analyzed ionograms from 21:00 UT (18:00 LT) to 09:00 UT (06:00 LT). The raw data was provided by the EMBRACE (Estudo e Monitoramento BRAsileiro de Clima Espacial) http://www2.inpe.br/climaespacial/portal/en/.

Raw data were obtained and processed into RSF and SAO files to generate ionograms for statistical analysis during the descending phase of cycle 24. As the spread F was identified, it was classified as RSF, FSF as well as the start and end time for each night of observation. The total interval of observation of the Digisonde from sunset to dawn (21:00 - 09:00 UT) was calculated by counting the total minutes of Spread F (Range and Frequency) for each month.

Table 5.1 shows the statistical results of how the monthly calculation was done, thus given by:

Occurrence rate = Number of hour of spread F type/Number of hour of Operation X 100.

For instance a case study using January month, note that the procedure is the same for the other month (minute):

$$\frac{7850}{15120}X100 = 52\%RSF \tag{4.7}$$

$$\frac{1350}{15120}X100 = 9\%FSF \tag{4.8}$$

Table 5.2 shows the statistical results of how the seasonal calculation was done, thus given by:

Occurrence rate: Total number of spread F type in each season /Total number of hour of Operation X 100.

For instance a case study using Summer solstice (Nov, Dec 2017) and (JAN, FEB

2018), note that the procedure is the same for the other season:

$$\frac{8960 + 9550 + 7850 + 5160}{17280 + 20160 + 15120 + 12240} X100 = 25\% RSF \tag{4.9}$$

$$\frac{4030 + 5480 + 1350 + 6010}{17280 + 20160 + 15120 + 12240} X100 = 14\% FSF \tag{4.10}$$

The spread-F identification were classified as frequency spread-F (FSF) and range spread-F (RSF) by observing every 30 mins window resolution on the ionogram. Table 4.1 shows the start and end time of spread-F on day 1 and 2 of April as case study, note that the procedure is the same for the other month:

Table 4.1 - Spread F identification (Range and Frequency) on ionogram in Belem 2018.

Equatorial Region (Belem)	Begin Time (UT)	End Time (UT)	Type of Spread F	Number of hour of Spread F (minutes)
April 1-2	00:40	07:00	FSF	460F
April 2-3	22:40	00:00	RSF	80R

We considered Figure 5.1 Vsw: Solar Wind Speed, in km/s, |B|: Interplanetary Magnetic Field, |B|, in nT; Sym H: the Ring Current index, in nT; Kp: geomagnetic index kp as the possible events for influencing the Spread F signatures during the period of studied and was taken from https://omniweb.gsfc.nasa.gov/ and Earth´s magnetometer.

Distribution of Equatorial spread-F of Range start time were performed as; P = Number of occurrence in each time bin in each month / Total number of spread-F in that month in any time x 100. For instance a case study for start time occurrence rate considering April (for example 21:00-21:59);

$$\frac{7}{17} = 41.2\% \tag{4.11}$$

Note that, the procedure is the same for each time bin of the month.

The observational datasets and compared spread-F probability of IRI Model were performed as; Number of spread F cases in each time / Number of ionograms of the whole month for each time. For case study, calculating the Spread F probability of January (at around 20 LT);

$$\frac{12}{21} = 0.571 \tag{4.12}$$

Note that, the procedure is the same for each time bin of the month.

5 RESULTS AND DISCUSSION

5.1 Introduction

In this chapter, we present the results on the investigation of the Brazilian equatorial spread-F during solar minimum 2018. For this purpose, it was analyzed ionospheric data taken from a Digisonde installed at Belem, (BL; 48°W, 1.43°S; Dip: -2.6°), from December 2017 to December 2018. The characteristics and statistical occurrences rate of spread-F were investigated to reveal the monthly and seasonal variation of the RSF and FSF and their dependence on solar activity and magnetic activity is being discussed thoroughly.

The solar minimum 2018 was characterized by a solar flux F10.7 mean at ≈ 69 SFU, where $1SFU = 10^{-22}\ Wm^{-2}s^{-1}$. Intense or severe geomagnetic storms are not much expectable to occur in 2018. However, some weak-to-moderate geomagnetic storms were observed, mostly associated with the occurrence of High-Speed Solar Wind Streams, HSSWSs (Vsw > 400 km/s) and Corotating interactions regions, CIRs.

Figure 5.1 shows, from top to bottom panels: Vsw: Solar Wind Speed, in km/s, |B|: Interplanetary Magnetic Field, |B|, in nT; Sym H: the Ring Current index, in nT; Kp: global geomagnetic Kp index taken from measurements at L1 point, at 1 AU, by the satellite ACE and available in https://omniweb.gsfc.nasa.gov/ and Earth´s magnetometer. Several events of HSSWSs can be seen as increases of Vsw over than 400 km/s, associated with the enhanced bulk magnetic field, |B|. The only intense storm was observed in August 2018 and it was associated with ICME events, for which SymH attained a value of ≈ -224 nT. The dotted horizontal blue lines highlight the average Vsw (400km/s); the moderate storm inferior limit, ≈ -50 nT; the disturbed kp, ≈ 4 and the mean solar flux, F10.7 in 2018, is ≈ 69 SFU.

Figure 5.1 - Solar and Geomagnetic Activity in 2018.

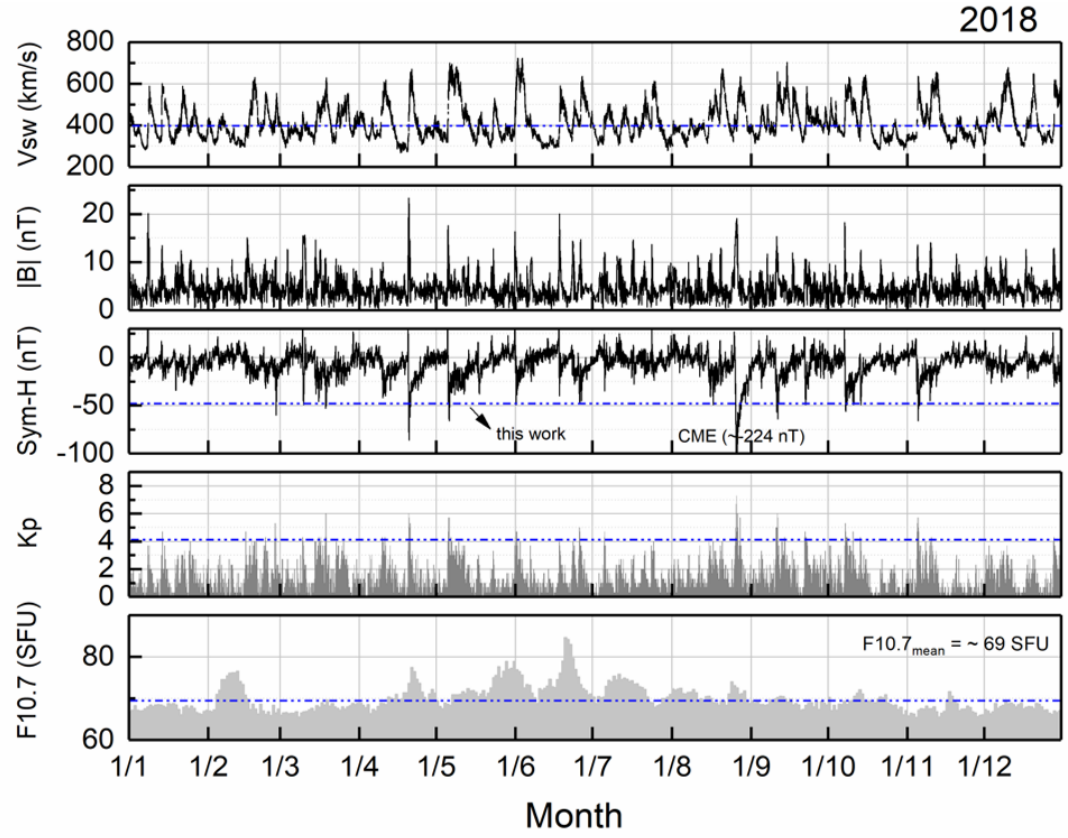

In order to investigate the Brazilian Equatorial spread-F during solar minimum 2018 and the possible influence of geomagnetic storms on their features, a statistical study of spread-F was performed. The first step was to identify by means of ionograms visual analyses, the occurrence, the pattern, the start time, and the end time of spread-F for each night in 2018. Figure 5.2 presents a sequence of ionograms with the main patterns of spread-F observed over the equatorial region, in Belém (dip lat:). Note that, as explained in chapter 3, there are two main patterns of spread-F: Range and Frequency, being Mixed spread-F a composite of both. Oblique spread-F refers to directional reference, and can include the former ones.

Figure 5.2 - Ionograms registered over the equatorial region at Belem showing different spread-F patterns of spread-F: A) range B) frequency; C) oblique echoes; D) mixed.

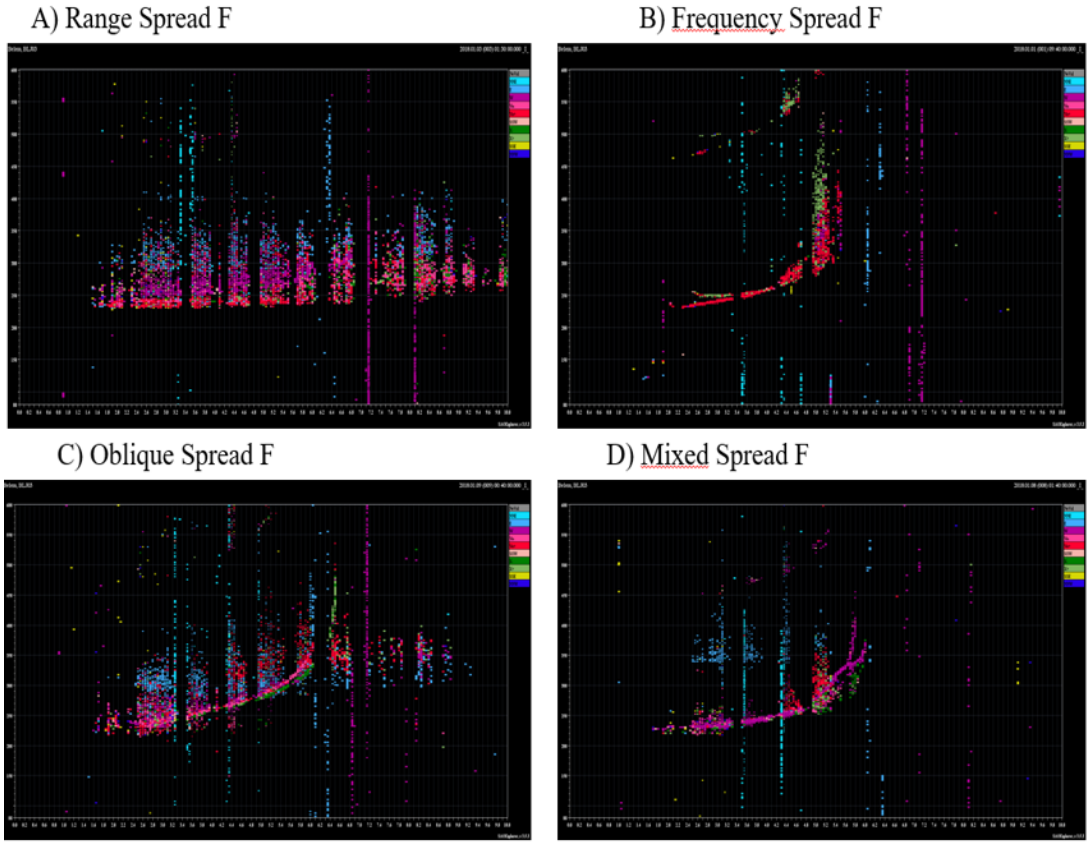

After carefully analyzing hundreds of ionograms, the most important information was registered. Table 5.1 shows the necessary information to perform the statistics of spread-F occurrence. It is shown the total interval of spread-F occurrence (in minutes), the whole interval of Digisonde operation/observation; and the percentile calculated from these data.

Table 5.1 - The time interval for each type of spread-F (RSF and FSF, in minutes) from November 2017 to December 2018.

Months	Total time of Spread-F Observation (R, F) (minutes)	Total time of Observation of Digisonde (21:00 - 09:00 UT) (minutes)	Occurrence rate % = N. of hours of Spread F type /N. of hours of Operation X 100% (R, F)
November	Range = 8960 Frequency = 4030	24 x 720 = 17280	52 23
December	Range = 9550 Frequency = 5480	28 x 720 = 20160	47 27
January	Range =7850 Frequency = 1350	21 x 720 = 15120	52 09
February	Range = 5160 Frequency = 6010	28 x 720 = 20160	26 30
March	Range = 4970 Frequency = 8020	30 x 720 = 21600	23 37
April	Range = 5000 Frequency = 6210	28 x 720 = 20160	25 31
May	Range = 4260 Frequency = 2120	27 x 720 = 19400	22 11
June	Range = 1310 Frequency = 3830	22 x 720 = 15840	08 24
July	Range = 2660 Frequency = 2250	30 x 720 = 21600	12 10
August	Range = 2190 Frequency = 800	15 x 720 = 10800	20 07
September	Range = 2300 Frequency = 3650	12 x 720 = 8640	26 42
October	Range = 2490 Frequency = 6560	19 x 720 = 13680	20 48
November	Range = 3400 Frequency = 3050	13 x 720 = 9360	36 33
December	Range = 1570 Frequency = 1520	8 x 720 = 5760	27 26

5.2 Monthly Spread F occurrence rate

Figure 5.3 presents the monthly occurrence rate of spread-F over Belem in 2018. top panel, in black: Range spread-F: Bottom panel, in red: Frequency spread-F.

Figure 5.3 - Occurrence rate for Range spread-F (top panel in black), and Frequency spread-F (bottom panel in red).

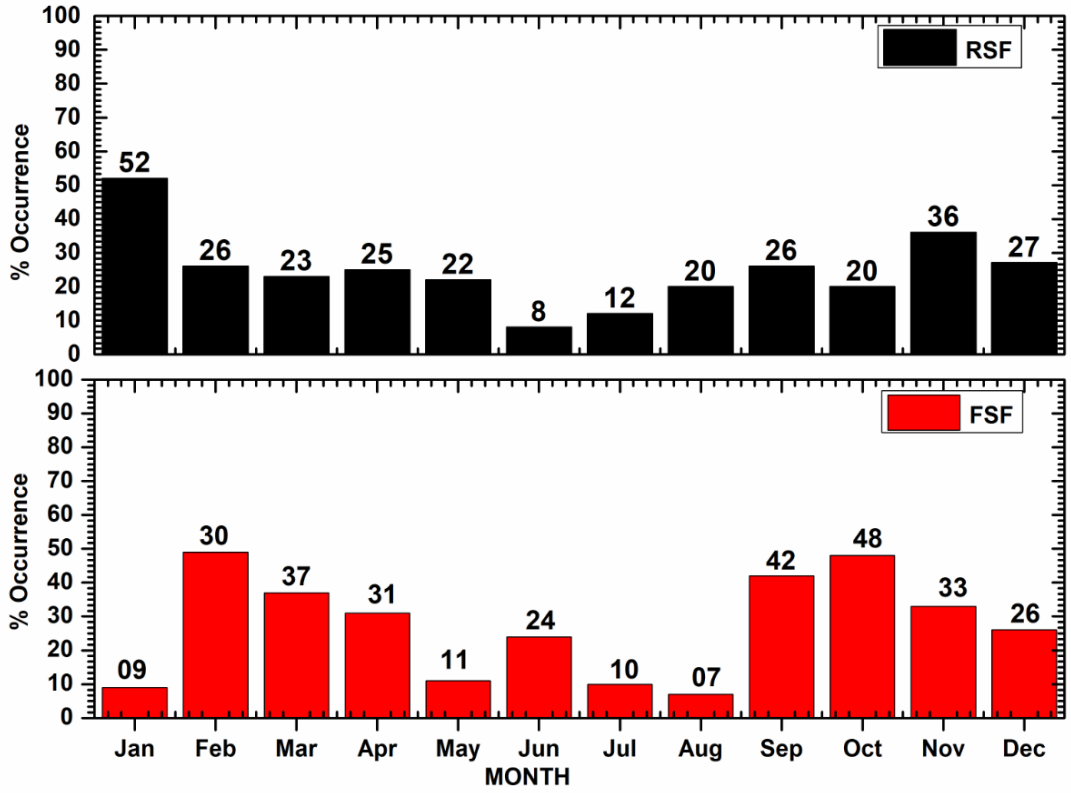

The highest occurrence rate for RAnge Spread-F was observed in January at ≈ 52%, followed by November at ≈ 36% and least in June at 8%. On the other hand, the Frequency spread-F occurrence has peaked during October at 48%, followed by September at ≈ 42%. The lowest occurrence rate was recorded in August, at ≈ 7%. Range Spread-F occurrence rate was maximum in Summer and Equinoctial months. The minimum was observed in Winter Solstice. Spread-F signatures were seen to appear in almost all the months with a strong seasonal variation. Here, although there are several spread-F but this present work focus more on RSF. The statistics analysis deducted above clearly showed that highest spread-F peak was generally centered on RSF. It is generally agreed that large scale plasma depletions are initially generated in the F region bottom side by the action of the gravitational Rayleigh Taylor instability mechanism in conjunction with some other disturbance sources such as gravity waves (Kelley et al. (1981)), zonal winds (Kelley (1985),

electric fields (Hansom et al. (1986)) and vertical winds (Raghavarao et al. (1987)). Furthermore, according to MA (2001) post-sunset spread-F are generated under the favorable sunset electrodynamics conditions of the ambient ionosphere, of which the most basic requirement is the evening uplift of the F-layer produced by the action of enhanced zonal (eastward) electric Field, widely known as the Prereversal enhancement, PRE.

Plasma irregularities, restricted to the F-layer bottomside, below the F-layer peak height, are called bottomside spread-F. If they reach the topside, they are referred as Equatorial Plasma Bubbles, EPBs. Spread-F is the generic term used by the authors to describe F-region irregularities. Range spread-F generally appear at the lowest edge of F-layer trace and are Preceded by a satellite trace. Frequency spread-F appear at the highest frequency edge and are associated with smaller scales irregularities. The Frequency spread-F generally appears as the latter development of the F-region irregularities. They are also believed to be associated with patches of ionization propagating eastward MacDougall et al. (1998). The magnitude of the daytime electric field is determined by the winds in the E-region, in the night E-region vanishes, F-region controls the electrodynamics of the ionosphere. In other words, F layer traces that show spread in range/height is range type spread-F (RSF), are known to be associated with developing, or developed, plasma bubble event, whereas the spread-F in frequency observed near the critical frequency of the layer, known as frequency type spread-F (FSF) are associated with narrow-spectrum irregularities that occur near the peak of the F layer, and not due to an unstable, or a potentially unstable, flux tube. The database used to achieve the results in Figure 5.3 included all days of observations and as such, it contains both quiet days and magnetically disturbed intervals. Note that there were missing data in some of the month. The Digisonde sounds the ionosphere using pulsed electromagnetic waves, from 1 to 20 MHz, registering the reflected echoes. The data was taken at 10 or 15 minutes time resolution. The morphological features of post-sunset equatorial spread-F have been extensively studied, including its dependence on solar and magnetic activities, season, day-to-day variability, longitude, latitude, and local time Abdu et al. (1981), Abdu et al. (1983), Li et al. (2011). During the spread-F season in Brazil, between October and March, the evening pre-reversal enhancement in the zonal electric field, and the F-layer vertical drift attains large values and range type spread-F is observed in equatorial ionograms, followed by their appearance at the crest region of the Equatorial ionization anomaly, EIA Abdu et al. (1998). The poor alignment between the sunset terminator and the magnetic field lines during the June solstice in Brazil is responsible for the low occurrence rate of post-sunset spread-F/EPBs since the

vertical plasma drifts are very weak. Also empirical representation of the equatorial spread-F (ESF) statistics using IRI model during quiet-time in the Brazilian longitude sector (Fortaleza and low latitude site Cachoeira Paulista) indicated that plasma bubble occurrence attain larger values in summer months (centered around December) than in equinoctial months (March and September) and minimum in winter months Abdu et al. (2003). Studies by Sobral et al. (2002) indicated that over Cachoeira Paulista EPBs shows a maximum rate of 86% in January and 11% in May and in addition presented that seasonal pattern shows up as broad a maximum and a minimum centered around the summer and winter months, respectively. During high-solar activity the maximum extends from September to April and for the low-activity period extends from October to March. To verify the seasonal behavior of the Equatorial spread-F, it was performed a statistical analysis considering the South Hemisphere: Summer solstice (Dec-Jan), Autumn Equinoxes (March-April), winter solstice (May-August), and Spring Equinox (September-October). Table 5.2 shows the statistical interval of spread-F; RSF and FSF (in minutes), the total number of hours of observation of the Digisonde, and the percentage occurrence rate in each respective season.

Table 5.2 - Seasonal Occurrence rate of spread-F.

Seasons	Months	Total number of Spread F in minutes(R, F)	Total time of Observation of Digisonde (21:00 - 09:00 UT) minutes	Occurrence rate%
Summer Solstice	Nov,Dec (2017) & Jan,Feb (2018)	Range =18100 Frequency =9920	17280 + 20160+ 15120 + 12240 = 72720	25 14
Autumn Equinox	Mar & Apr	Range = 9970 Frequency = 14230	21600 + 20160 = 41760	23 34
Winter Solstice	May,Jun Jul& Aug	Range = 10420 Frequency = 9000	19440 + 15840 + 21600 + 10800 = 67680	15 13
Spring Equinox	Sept & Oct	Range = 4790 Frequency = 10210	8640 + 13680 = 22320	22 46

Figure 5.4 The seasonal occurrence rate of the spread-F over Belem from November 2017 to December 2018. The top black panel: Range spread-F and bottom red panel: Frequency spread-F.

Figure 5.4 - Seasonal Occurrence Rate of spread-F in 2018. Top panel: Range spread-F, Bottom panel: Frequency spreas-F.

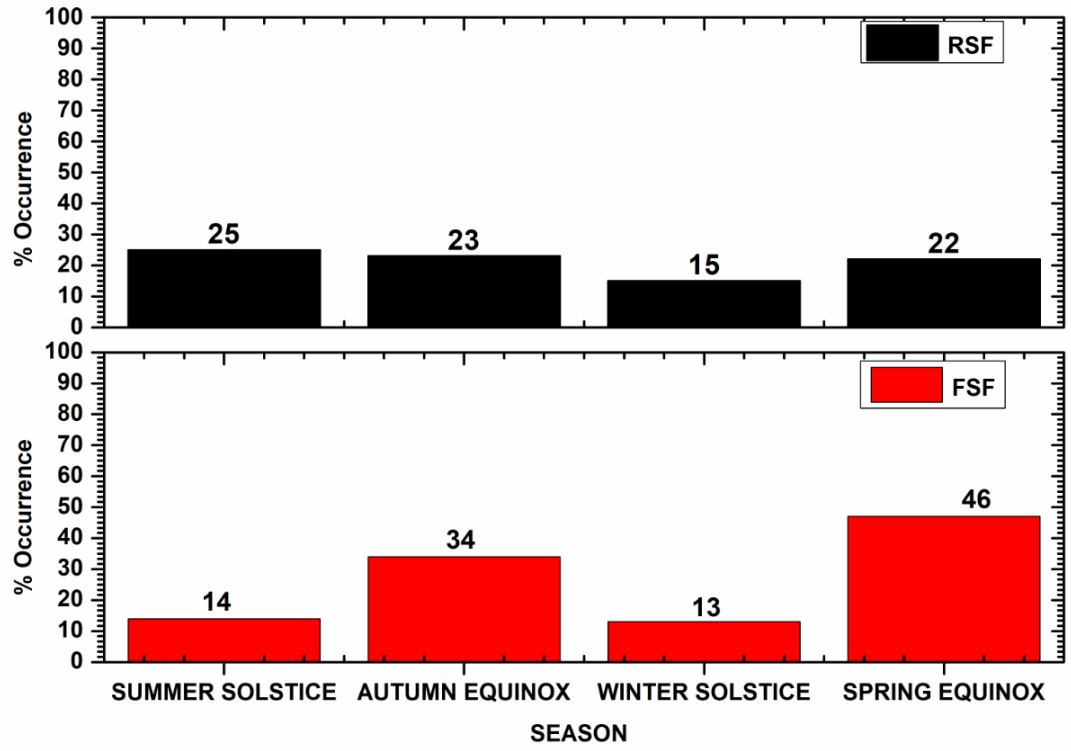

Figure 5.4 shows the seasonal percentage occurrence rate obtained for RSF and FSF from November 2017 to December 2018. The highest occurrence rate of Range spread-F occurs in Summer Solstice, 25% and the lowest occurrence rate of spread-F was observed during the winter solstice, at 15% thus, the occurrence rate was 25% for the Summer followed by Autumn equinox at 23% and the lowest occurrence rate in winter at 15%. On the other hand, the Frequency spread-F occurrence rate presents the highest occurrence rate at 46% during equinoxes, followed by Autumn equinox at 23% and least at 13% for Winter solstice. From the figure, it can be noticed that; The result obtained for summer solstice, especially in FSF is observed to have a low rate, for the reason being that during the period of observation, most

of the events appeared to be range and limited data gathered. In most of the month, it was incapable to identify the trace of FSF. The statistics of ESF occurrence are known to present significant variation with the season and such variation is known to be controlled by longitude-dependent geomagnetic declination angle as was first pointed out by Abdu et al. (1981). The seasonal variation of spread-F occurrence revealed in these results, as a minimum of occurrence in winter months (that is, May-August) with a broad maximum centered around equinoctial and summer months (that is, from October to March), is consistent with that obtained by Abdu et al. (1981) and Sobral et al. (2002) respectively. In addition, agrees with the statistical results obtained from extensive ionosonde data over Cachoeira Paulista investigated by (Abdu et al. (1998). This seasonal behavior is well explained in terms of the alignment of the solar terminator with the magnetic meridian. This relationship was also studied by (TSUNODA, 1985).

Equatorial spread-F in the Brazilian longitudinal sector is characterized by a large negative magnetic declination and has high occurrence rates during the local Summer and equinoctial months Abdu et al. (1981). Chandra et al. (2003) analyzed the spread-F occurrences rate at Cachoeira Paulista in Brazil and indicated that maximum RSF in Summer during low-sunspot years. Furthermore, Abdu et al. (1983) performed a comparative study of the occurrence of spread-F over Fortaleza and Cachoeira Paulista during maximum solar activity epoch. They observed very low probabilities of frequency type spread-F and no Range type spread-F occurrence during June solstice without the respective Spread F types at the equatorial site. Also, Chapagain et al. (2009) reported the very low occurrence of spread-F/plumes over Jicamarca during June solstice using coherent and incoherent scatter radar data. Furthermore, Dabas et al. (2007) also stated high occurrence rate of RSF occurred mostly in equinoxes and at post-sunset. It is observed that the Range spread-F presents a higher occurrence rate in Summer solstices and lower during winter.

(TSUNODA, 1985) also observed that Frequency spread-F shows a higher occurrence rate in spring equinox and lower in winter Solstice.

The results obtained in this work seem to agree with these authors. It is worth noting that the statistics of ESF occurrence rate are known to present significant seasonal variation patterns being different for different longitude sectors of the globe. Such seasonal variation is known to be controlled by longitude-dependent geomagnetic declination angle as was first pointed out by Abdu et al. (1981). The behavior of irregularities in Summer and Winter can be explained in terms of the late time

of reversal of PRE at the dip equator. According to (FEJER et al., 1999) the later (earlier) time of reversal of the PRE which occurs in the local summer (winter) at the magnetic equator favors (inhibits) the occurrence of irregularities. The generation of RSF over the magnetic equator requires three conditions as suggested by (RASTOGI, 1980): (i) a large plasma gradient in the ionosphere, a nighttime condition, (ii) an eastward electric horizontal electric field, basically extension of daytime condition, and (iii) maintenance of the two above conditions for a period of about half an hour or more and under these conditions, he explained the abnormal seasonal variation of the occurrence of equatorial spread-F in the American zone.

5.3 Onset time of spread-F occurrence rate duration during 2018.

In order to investigate the spread-F features during solar minimum 2018, it was performed an analysis of the Spread F onset time for each day of each month.

Table 5.3 The statistical study of spread-F start time occurrence rate. These was performed by observing the spread-F start time for every 60 minutes on the ionograms.

Table 5.3 - Spread F start time.

Months	18:00-18:59 (LT)	19:00-19:59 (LT)	20:00-20:59 (LT)	21:00-21:59 (LT)	22:00-22:59 (LT)	23:00-23:59 (LT)	00:00-06:00 (LT)
January	2	4	5	13	0	0	0
February	0	3	2	9	1	0	4
March	0	2	4	6	0	0	1
April	0	2	4	7	2	0	2
May	0	0	0	6	1	1	1
June	1	3	0	3	0	0	0
July	0	2	0	5	3	1	2
August	3	0	0	5	0	1	0
September	0	3	0	3	0	1	1
October	0	6	2	5	0	0	4
November	1	7	1	8	0	0	0
December	0	3	0	4	0	0	3

The distribution of time occurrence percentiles was plotted as a function month for different local times of spread-F, starting from 18 LT to 06:00 LT. Each time bin is

defined as the interval of spread-F observation, from post-sunset to pre-dawn/dawn (18:00 - 06:00 LT). The calculation of the percentage (P) is mathematically expressed as:

P=(NT/TM) x 100;

where NT = number of occurrences in each time bin in each month

TM = total number of spread-Fs in that month at any time

Figure 5.5 - Distribution of spread-F start time of Belem 2018.

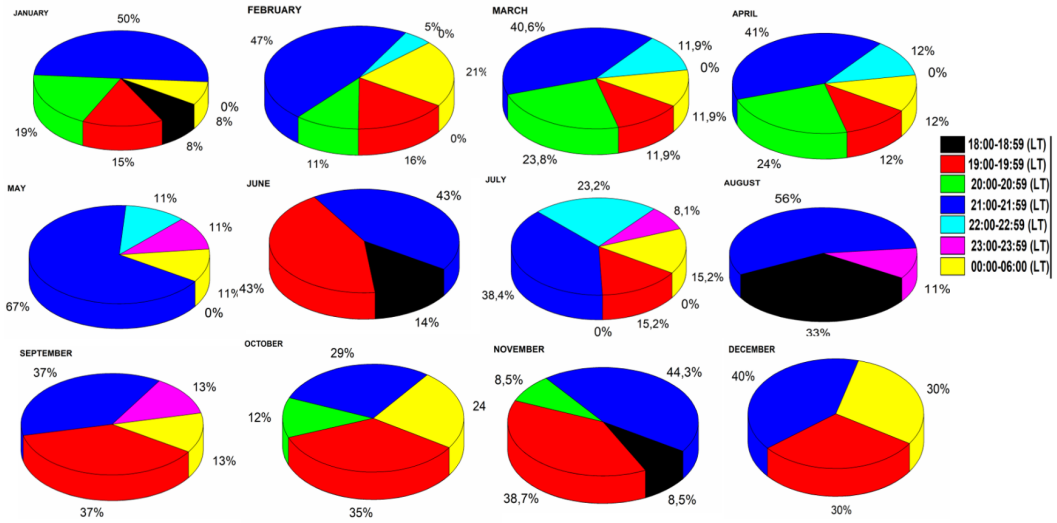

It is observed that the spread-F start time is mostly distributed between 19:00 and 22:00 LT with the most cases occurred at around 21:00 LT (except in October), followed by the interval 19:00 to 20:59 during the first months of the year (January to April). Post midnight onset times are seen during Equinoxes and Summer and less frequent during Winter Solstice. Between September and
December, the onset time around 19:00 - 19:59 is comparable to most common, at 21:00 LT. The postmidnight irregularities in summer solstice are attributed to late R-T instability and strong upward drift capable of lifting the F layer. The equatorial F region evening vertical drift, due to pre-reversal electric field enhancement, is an important condition for the spread- F/plasma bubble irregularity generation, which

is more frequent during summer-equinoctial months over South America Abdu et al. (1981). They are generally much weaker and much less frequent than the post-sunset events. The post sunset spread-F are generally thought to be associated with the evening prereversal enhancements (PRE) of vertical drift velocity Fejer et al. (1999). Under the action of the PRE, the ionosphere is rapidly elevated to higher altitudes, where collision frequencies are low, favoring the growth of the irregularities by the R-T instability mechanism. PRE is an enhancement in the eastward electric field in the E-region of the ionosphere that is caused by a high conductivity gradient across the day-night terminator during the post-sunset hours Farley et al. (1986). This enhancement occurs just before the reversal of eastward electric field during the daytime to westward during nighttime around 20:00 LT (TSUNODA, 1985). On the other hand, Post midnight was less frequent in the equatorial region during June Solstice. Also, Li et al. (2011) showed that the post-midnight spread-F for June months over Jicamarca reached a peak near 03:00 hrs LT. MA (2012) showed that during December solstice, the post-midnight spread-F occurrence rate increases from high solar flux to low solar flux years, being 50% and 90% respectively near 03:00 hrs LT. The post-midnight irregularities occur, in general, more frequently during solar minimum years than during solar maximum years. Candido et al (2011) observed PMSF at low latitudes occurred ≈80% of the nights during solar minimum. MA (2012) showed that during solar maximum, the irregularity development begins in the early post-sunset hours near 19:00-20:00 hrs LT, which is generally tied to the pre-reversal vertical drift that usually has large amplitudes, and the irregularities peak around 22:00 hrs LT.

5.4 Equatorial spread-F probability: observations and international reference Ionosphere IRI modeling.

In this section, we compare the Brazilian Equatorial spread-F observations with the spread-F probability provided by the International Reference Ionosphere, IRI model. IRI is an empirical standard model of the ionosphere, based on all available data sources in the world: The major data sources are the worldwide network of ionosondes, the powerful incoherent scatter radars, topside sounders, satellites, etc. For a given location, time, and date `https://ccmc.gsfc.nasa.gov/modelweb/models/iri2012_vitmo.php`, IRI provides monthly averages of the electron density, electron temperature, ion temperature, and ion composition in the altitude range from 50 km to 2000 km. Additionally, parameters given by IRI include the Total Electron Content (TEC; a user can select the starting and ending height of the integral), the occurrence probability for spread-F and also the F1-region, and the equatorial ver-

tical ion drift. The same hourly time was considered for both IRI model and Spread F occurrence percentage features for each month.

Table 5.4 shows the observed spread-F cases number for each hour in each month. The spread-F probability is obtained with the model of Abdu et al. (2003) based on ionosonde measurements from the Brazilian longitude sector. Since the spread-F occurs from evening to the morning we chose distribution at l-hour interval between 18 and 06 LT.

Table 5.4 - Monthly observed Spread F datasets values in each time.

Months	Observed Datasets (18 - 06 LT)												
	18	19	20	21	22	23	24	01	02	03	04	05	06
January	0	1	12	25	16	16	16	14	10	10	8	2	2
February	1	1	5	17	13	11	9	11	7	7	5	2	1
March	0	1	8	14	12	10	11	10	9	9	8	8	6
April	0	1	8	13	10	9	9	9	9	8	1	1	4
May	0	0	1	11	11	10	9	9	6	4	4	4	2
June	0	1	3	6	3	3	2	2	1	0	0	0	0
July	0	1	6	8	8	8	9	8	4	1	0	0	0
August	0	3	5	10	6	7	7	2	0	0	0	0	0
September	0	0	2	5	3	4	4	4	3	3	2	1	1
October	0	0	6	12	6	4	5	4	3	4	3	2	2
November	2	19	22	23	21	17	23	21	19	19	12	8	3
December	3	14	25	24	24	23	25	25	19	17	10	4	5

The spread-F probability was performed mathematically as;

Number of spread-F cases in each time/Number of ionograms of the whole month for each time. IRI model running request as input data: the year initial time, the F10.7 monthly average, and date. The observed spread-F was only run once in each month using the IRI model. As a reference, day 15 was selected as the representative day for each month to infer the Spread-F Probability. The analysis was done by considering the data of Belem from November 2017 to October 2018. This period was considered due to the availability of data. Figure 5.6 shows the nocturnal local time occurrence rate of spread-F probability observed and predicted by IRI model each time in each month. The spread-F probability by IRI is based on Abdu's model, who in his turn performed a statistical study using 13 years of Digisonde data.

Figure 5.6 - Spread F probability comparison between IRI model and observed Spread F for the equatorial region, Belém, in 2018.

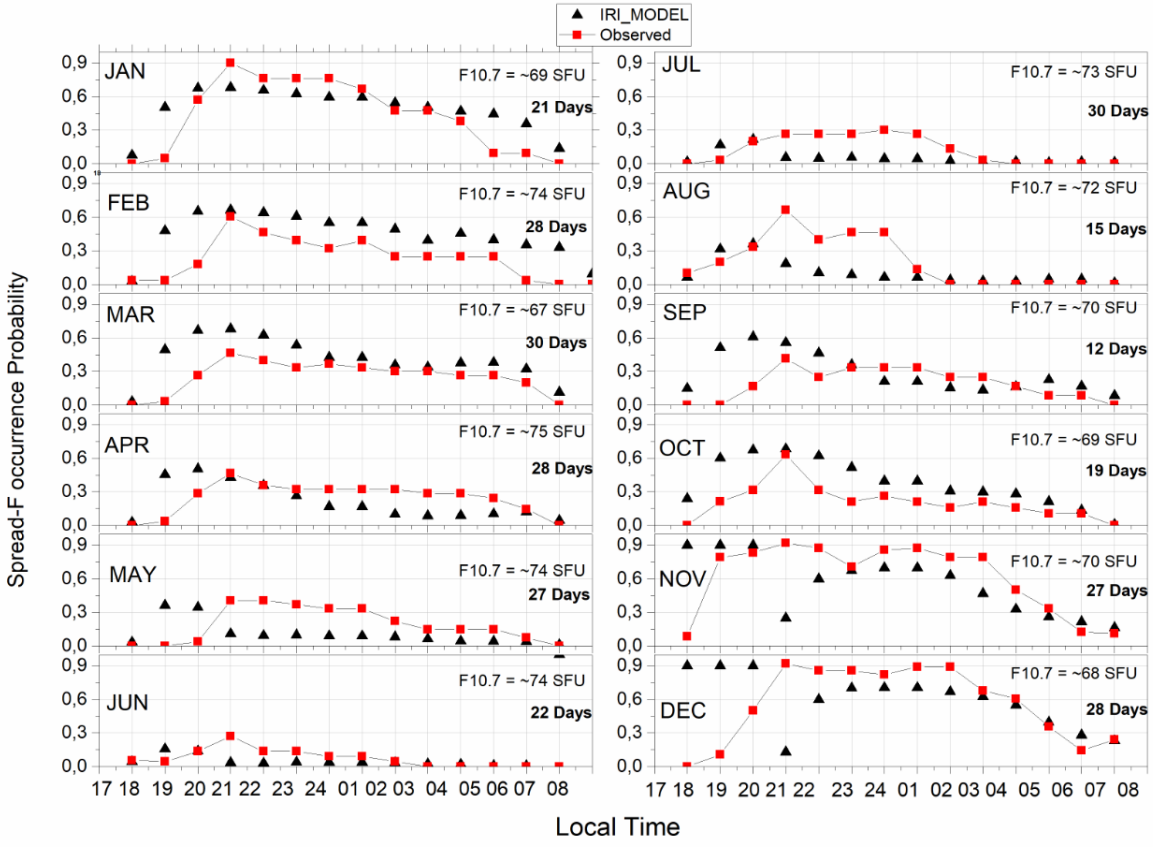

The solar flux F10.7 was observed to vary from each respective month but in general, the mean value was taken to be ≈ 69 SFU, indicating minimum solar activity conditions. In general, observed probability took from Digisonde data and IRI model presents a similar trend. However, IRI can overestimate or underestimate the spread-F occurrence in some times. The same hourly time was considered for both IRI model and Spread F occurrence percentage features for each month. In each month, the occurrence rate from a low value of 18LT increases rapidly to reach a pre-midnight maximum. However, the local time of the maximum is the same for each month, at around 21:00 LT. The monthly spread-F occurrence rate was higher in summer and equinoctial months and least recorded in winter months. However, observation in November and December present a unique pattern with high spread-F probability as compared to the other month. This is due to different periods thus, those months

are considered to be under solar maximum conditions. The results seem to agrees with Abdu et al. (2003) which stated that spread-F season extends from September to March for low solar flux values and for high solar flux values the season is a bit more extended to include the months of April and May as well. According to Batista e Abdu (2004) at the equatorial station, the most striking difference was on the location of the annual maximum (equinox– summer in the data, winter in the IRI model). In addition, the winter months show a short duration small percentage of occurrences close to post-sunset hours. The onset of spread-F over Belem occurs mostly from 19 to 21 LT.

5.5 Day-to-day variability of Equatorial spread-F – the role of geomagnetic storms during solar minimum

In previous Figure 5.3 and figure 5.4 it was discussed the long-term variability of the spread-F, such as its seasonal dependency, with maximum occurrence rate during December solstice and minimum during June Solstice. It was also addressed that the ionospheric conditions determined by the electrodynamics are of great importance on the development of spread-F/plasma irregularities over the equatorial region. In this section, it is analyzed the short-term day-to-day variability of equatorial spread-F during solar minimum 2018. The short-term day-to-day variability observed in the equatorial spread-F has been investigated by many authors and can be attributed to several factors: upward atmospheric gravity waves propagating at F-region, Prompt Penetration Electric Field, PPEF, and Disturbance Dynamo Electric Fields, DDEF, associated to distinct phases of geomagnetic disturbances and time occurrence, as well as to disturbed transequatorial winds (Abdu (2019). In this work, we analyze the possible influence of geomagnetic storms in 2018 on the equatorial spread-F in Brazil. Table 5.5 presents a list of geomagnetic storms during 2018, their intervals, strength, Kp max, and the driving mechanism.

Table 5.5 - Moderate-to-intense geomagnetic storms during 2018.

Months	Interval	Storm level	SymH min nT	Recovery phase Duration days	Kp max	Forcing
January	*		-	-	-	-
February	*		-	-	-	-
March	14-20	Moderate	-50	2d	6	CIR/HSS
April	20-25	Moderate	-84	5d	6	CIR/HSS
May	05-13	Moderate	-60	8d	6	CIR/HSS
June	25-28	Moderate	-49	2d	6	CIR/HSS
July	*	-	-	-	-	-
August	25-31	Intense	-174	6d	7	ICME
September	10-14	Moderate	-63	3d	6	CIR/HSS
	21-23	Moderate	-50	2d	5	CIR/HSS
October	07-13	Moderate	-53	7d	5	CIR/HSS
November	04-08	moderate	-50	4d	6	CIR/HSS
December	*	-	-	-	-	-

It is noticed for each month there is at least one moderate storm, except for January and February (weak disturbances), August (intense/CME storm), and December (weak storm). It is also observed that the recovery phase of the storms can last for many days. The main source of these storms is believed to be CIR/HSSs.

Figure 5.7 and Figure 5.8 present the SymH, F10.7, kp, the day-to-day occurrence, onset time, and duration of equatorial spread-F (Range: in blue and Frequency, in orange) during each month of 2018. It is possible to observe weak and moderate geomagnetic storms and the geomagnetic disturbance through kp.

Figure 5.7 - Geomagnetic and solar indices, SymH, F10.7 and kp, and spread-F occurrence and duration; Blue: Range spread-F; Red: Frequency spread-F; Black: Mixed spread-F (January to June).

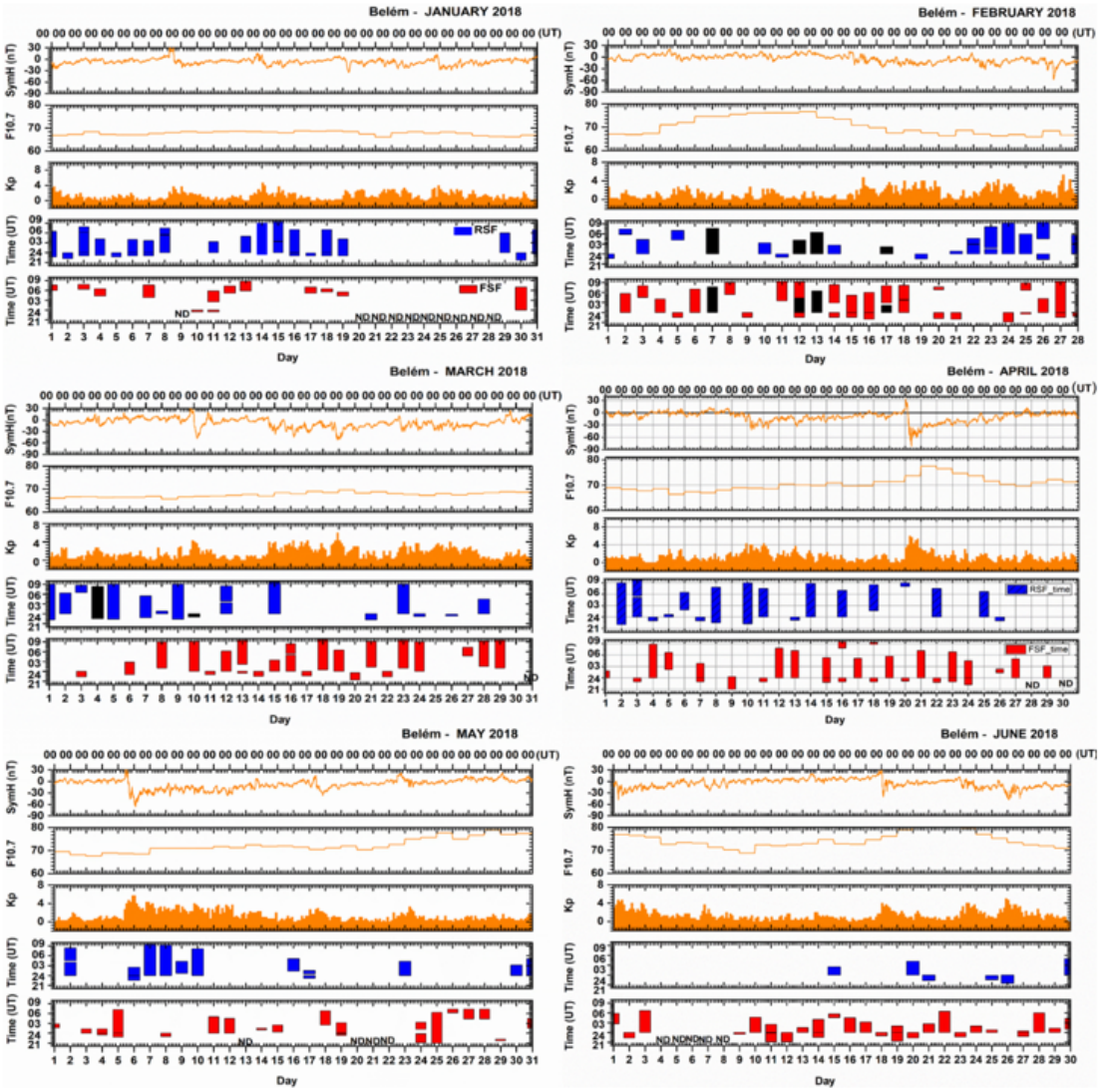

The solar flux, F10.7, is on average around 70 SFU, and some intensifications are also observed.

Figure 5.8 - Geomagnetic and solar indices, SymH, F10.7 and kp, and spread-F occurrence and duration; Blue: Range spread-F; Red: Frequency spread-F; Black: Mixed spread-F (July to December).

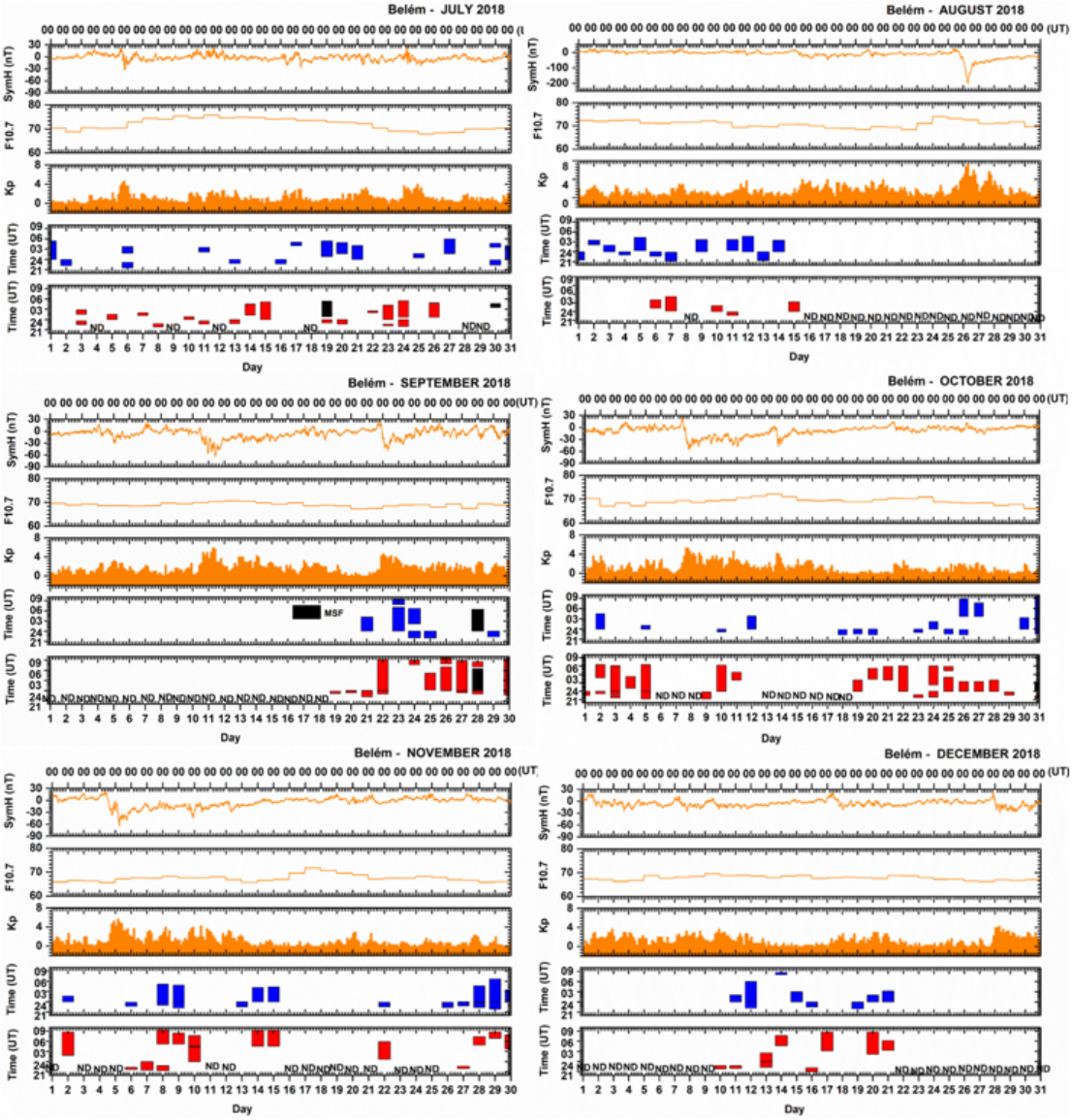

In general, it is noticed that both Range and Frequency spread-F (in blue) can occur during quiet and geomagnetic disturbed days, especially from January to April, which is strongly related to the seasonal variability discussed in the previous section. Additionally, spread-F duration is variable, being shorter during Winter Solstice. It

is observed that in some phases of the storms the spread-F is not observed. For instance, in the main phase of the storms on March 10 and April, 21 there are no spread-F occurrence. On the other hand, spread-F can be observed for some days during the long geomagnetic storm in May 2018, a month out of the spread-F season in Brazil (October-March). Notice, Figure 5.6 that the probability of spread-F occurrence predicted by IRI Model underestimated the observed spread-F probability in May, Unfortunately, during the second part of the year, there are long gaps of Digisonde data at the equatorial region in Belem, as seen in the graphs, and it was not possible to analyze the occurrence or not of spread-F for some periods.

In order to better understand the influence of a moderate geomagnetic storm on the Brazilian equatorial spread-F during solar minimum, its was selected the geomagnetic storm which occurred on May 05-13.

Figure 5.9 shows, from top to bottom panel, the solar wind speed, Vsw (km/s); the proton density, Np ($\frac{1}{cm^3}$); the interplanetary magnetic field, |B| (nt); the horizontal geomagnetic field component, the geomagnetic index, kp; and the solar flux index, F10.7 (SFU), in GSM coordinate systems for May 05-08, 2018. Vsw, Np, |B|, F10.7 were provided by the measurements on probes onboard ACE satellite at 1 AU, and available on OMNI web NASA website in: https://omniweb.gsfc.nasa.gov/form/dx1.html. It is observed that Vsw is around 600 km/s for many days, which is the signature of a HSSs event. Np peak is the signature of a CIR, a narrow region of compressed plasma created by the interaction of slow-high speed streams in the interplanetary space. B magnitude is around 15 nT. The initial phase of the storm was on May 05 $\approx$ 10:00 UT; the main phase lasts from May 05 at 16:00 to May 06 at $\approx$ 01:50 UT, when SymH reached its minimum, at $\approx$ -56 nT. The recovery phase is from 01:50 UT May 06 to 18:00 UT May 13 (shown Figure 5.7). Kp was on average 4 (disturbed) for many days, and 6 during the main phase.

Figure 5.9 - Solar, Interplanetary, and geomagnetic indices and parameters variation during 05-08 May 2018.

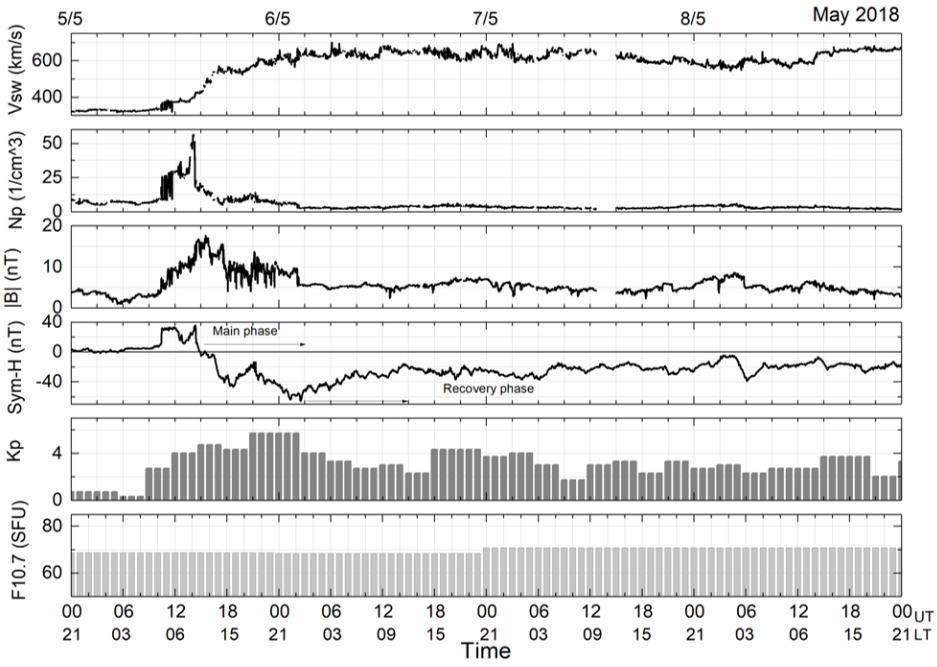

The ionospheric response to this geomagnetic storm can be seen in Figure 5.10 From the top to the bottom panel are presented: 1-min SymH, Bz (nT) and Ey(mV/m), and the ionospheric parameters taken from the Digisonde at Belem: the virtual F-region height, h^IF (km); F-layer peak height, hmF2 (km), and the plasma critical frequency, foF2 (MHz) taken from Digisonde measurements. Data were carefully manually processed using SAO Explorer. The average of the five quietest days, 5QD (based on the kp index provided at `http://wdc.kugi.kyoto-u.ac.jp/qddays/`) of each ionospheric parameter was also calculated for comparison. It is noticed a sudden F-region uplift at $\approx$ 22:00 UT (19:00 LT) which peak at $\approx$ 02:00 LT, for both h^IF and hmF2, followed by a decrease of foF2 in comparison to their 5QD average. Indeed, the foF2 average is lower than 2 MHz after local midnight, as indicated in Figure 5.10.

Figure 5.10 - Geomagnetic, interplanetary, and ionospheric parameters and indices during a moderate geomagnetic storm in May 2018.

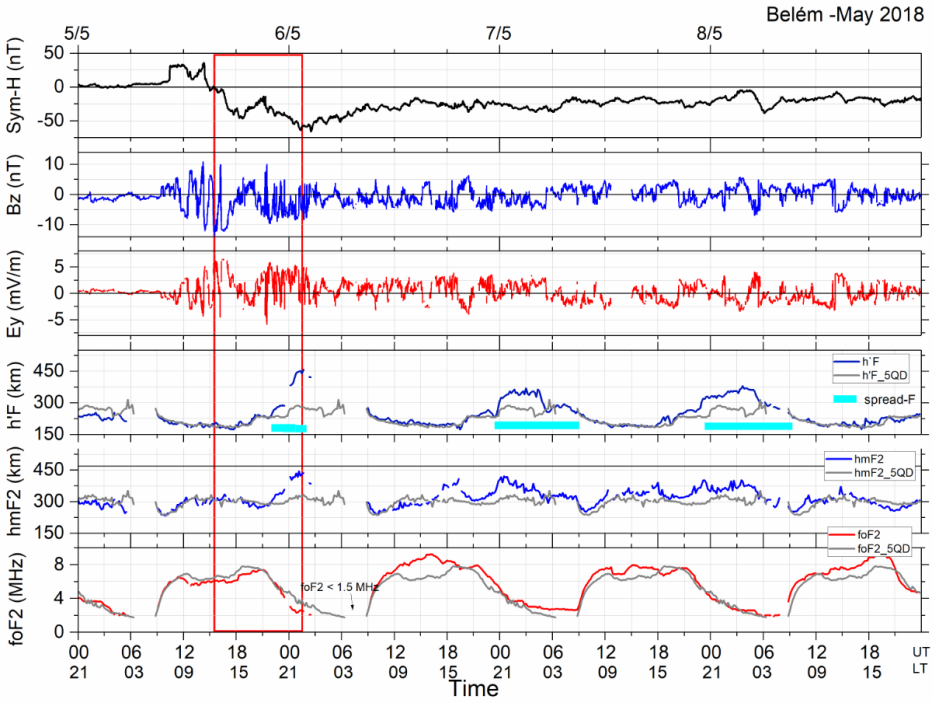

For completeness, Figure 5.11 presents a sequence of Directograms for the main phase and two recovery phase days of the storm. A Directogram is one of the Digisonde recording modes and is a graph of the space/time distribution of the spread-F reflected echoes Reinisch et al. (2005). The horizontal axis is the zonal West-East distance from the station, Belem, being the vertical echoes not present. It is observed the occurrence of spread-F echoes from irregularities at distances up to around 600 km at west or east of the instrument location. As expected, spread-F is firstly observed at equatorial region, in Belem, and has a short duration in the first night (main phase). Additionally, the spread-F is observed at around the north crest of EIA, at Boa Vista. This means that the spread-F reached the topside equatorial ionosphere and traveled to low latitudes, at Boa Vista. The well-defined reflected echoes at Boa Vista are probably associated with the higher plasma densities in the region (crest of EIA). It is important to address that is expected the irregularities/spread-F is developed first at Belem (located at the east of Boa Vista) and then propagates eastward. In this way, the spread-F observed at Boa Vista

can have developed at a equatorial location at west of Belem. This "unexpected" spread-F/Plasma Bubbles occurrence in May, can be favored by the sudden F-region uplift during a probable PPEF in the main phase of the storm (Bz < 0 and Ey >0). Spread-F was also observed during some days of the recovery phase, as seen in the Directograms. Notice that the parameters hmF2 and h^IF were higher than the 5QD in the recovery phase of the storm, which can be caused by disturbance dynamo electric fields, DDEF, during the recovery phase of the storms or by new and less intense PPEF (to be studied in a further investigation). Finally, it is observed that daytime foF2 was also intensified in the recovery phase shown in Figure 5.10.

As extensively studied by Fejer et al. (1999), the pre-reversal enhancement is absent. However, during geomagnetic storms, the vertical drifts can be strengthened by the action of prompt penetration electric fields at the equatorial region. Moreover, during the nighttime downward vertical drifts under solar minimum conditions, even a small disturbance can reverse and be favored. Becker-Guedes et al. (2004) indicated that the geomagnetic activity acted as an inhibitor during high SF occurrence months and as an initiator during low SF occurrence months. With these analyses we observed that a moderate geomagnetic storm caused by CIR/HSS can favor the occurrence of spread-F during periods out of the spread-F season in Brazil or at late night for several days, leading to the development of topside plasma irregularities, or plasma bubbles. It is possible that even the low occurrence of EPBs can be due to the influence of moderate geomagnetic disturbances. These results can be of interest for Space Weather prediction centers.

Figure 5.11 - Directograms for Belem and Boa Vista from 5 to 8 May 2018: Main phase (day 5-6) and the recovery phase (day 6-8) during geomagnetic storm.

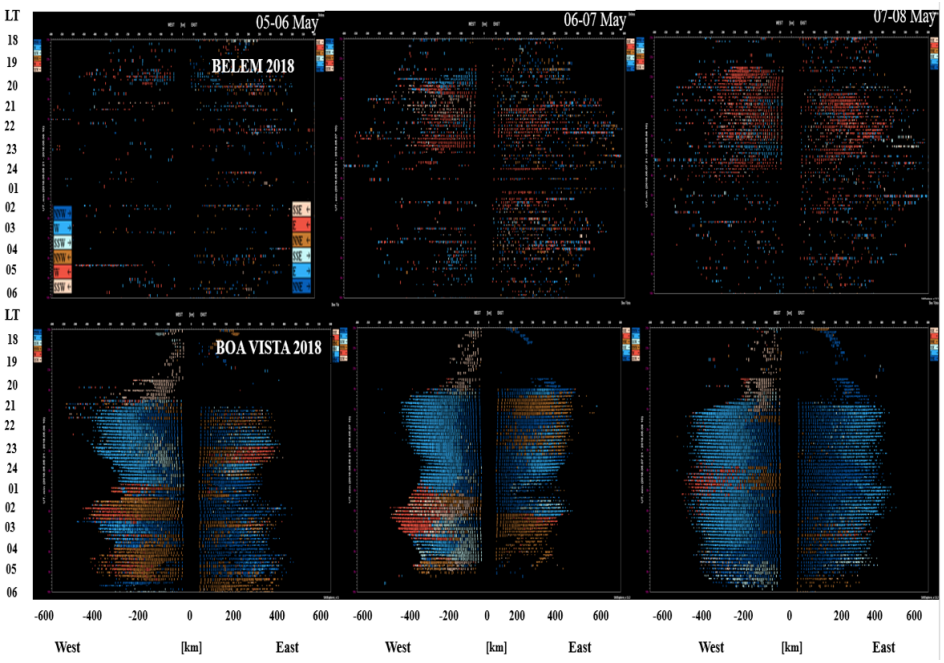

6 CONCLUSION

This work presented a study of the Brazilian equatorial spread-F during solar minimum 2018 using Digisonde data. A statistical study was performed based on the analysis of thousands of ionograms registered in Belem, PA. The spread-F probability observed and calculated by International Reference Ionosphere Model, IRI, was compared. Besides, the day-to-day variability was analyzed for each month. A case study was performed to investigate the role of a moderate geomagnetic storm on the equatorial spread-F. The main findings and conclusions of this study are summarized as follow:

- The main patterns of equatorial spread-F are Range and Frequency, followed by Mixed spread-F, a combination of both previous spread-F types;
- The Brazilian equatorial spread-F occurrence rate during solar minimum has a strong seasonal dependency with peaks in Summer Solstice and Equinoxes and minimum at June solstice;
- The spread-F onset time during solar minimum was mostly at around 21:00 LT;
- Post midnight equatorial spread-F occur mainly in December solstice;
- Equatorial spread-F duration is variable, lasting for tens of minutes to several hours, except in June Solstice, when the plasma density can be severely reduced with no reflected echoes in some pre-dawn intervals;
- Equatorial spread-F during solar minimum also presents a day-to-day variability, which can be caused by many factors. In this work, it was analyzed and noticed that moderate geomagnetic storms driven by CIR/HSS can influence the spread-F occurrence in a short-term variability, possibly associated with Prompt Penetration Electric Fields and Disturbance Dynamo Electric Fields;
- An intensified ExB vertical drift during a moderate geomagnetic storm can lead to the development of spread-F and Equatorial Plasma Bubbles, which can be observed at low latitudes, such as Boa Vista, around the north crest of EIA, even during a non-spread F season month;
- During the recovery phase of a moderate geomagnetic storm, plasma frequency/density can be intensified, probably due to the effects of DDEFs,

which may maintain the F-layer at higher altitudes, where the recombination rates are lower.

- The occurrence rate from a low value of 18LT increases rapidly to reach a pre-midnight maximum in all months. However, observed probability obtained from Digisonde data and IRI model present a similar trend.
- This work contributes to understanding space weather events during solar minimum and has the potential to be of interest for Space Weather studies and prediction centers.

REFERENCES

ABDU. Day-to-day and short-term variabilities in the equatorial plasma bubble/spread f irregularity seeding and development. **Progress in Earth and Planetary Science**, v. 6, n. 1, p. 1–22, 2019. 65

ABDU, M. Major phenomena of the equatorial ionosphere-thermosphere system under disturbed conditions. **Journal of Atmospheric and Solar-Terrestrial Physics**, v. 59, n. 13, p. 1505–1519, 1997. 29

ABDU, M.; BATISTA, I.; REINISCH, B.; SOUZA, J. D.; SOBRAL, J.; PEDERSEN, T.; MEDEIROS, A.; SCHUCH, N.; PAULA, E. D.; GROVES, K. Conjugate Point Equatorial Experiment (COPEX) campaign in Brazil: Electrodynamics highlights on spread F development conditions and day-to-day variability. **Journal of Geophysical Research: Space Physics**, v. 114, n. A4, 2009. 31

ABDU, M.; BITTENCOURT, J.; BATISTA, I. Magnetic declination control of the equatorial F region dynamo electric field development and spread F. **Journal of Geophysical Research: Space Physics**, v. 86, n. A13, p. 11443–11446, 1981. 14, 15, 19, 27, 35, 56, 59, 62

ABDU, M.; KHERANI, E.; BATISTA, I.; SOBRAL, J. Equatorial evening prereversal vertical drift and spread F suppression by disturbance penetration electric fields. **Geophysical Research Letters**, v. 36, n. 19, 2009. 2, 17, 25

ABDU, M.; MEDEIROS, R. de; NAKAMURA, Y. Latitudinal and magnetic flux tube extension of the equatorial spread F irregularities. **Journal of Geophysical Research: Space Physics**, v. 88, n. A6, p. 4861–4868, 1983. 56, 59

ABDU, M.; SOBRAL, J.; BATISTA, I.; RIOS, V.; MEDINA, C. Equatorial spread F occurrence statistics in the american longitudes: diurnal, seasonal and solar cycle variations. **Advances in Space Research**, v. 22, n. 6, p. 851–854, 1998. 1, 14, 27, 28, 56, 59

ABDU, M.; SOBRAL, J.; NELSON, O.; BATISTA, I. Solar cycle related range type spread F occurrence characteristics over equatorial and low latitude stations in brazil. **Journal of Atmospheric and Terrestrial Physics**, v. 47, n. 8-10, p. 901–905, 1985. 23, 27

ABDU, M.; SOUZA, J.; BATISTA, I.; SOBRAL, J. Equatorial spread F statistics and empirical representation for iri: a regional model for the brazilian longitude sector. **Advances in Space Research**, v. 31, n. 3, p. 703–716, 2003. 2, 24, 38, 57, 63, 65

AKASOFU, S.-I. The development of the auroral substorm. **Planetary and Space Science**, Elsevier, v. 12, n. 4, p. 273–282, 1964. 39

BAKER, W. Electric currents in the ionosphere-the atmospheric dynamo. **Philosophical Transactions of the Royal Society of London. Series A, Mathematical and Physical Sciences**, v. 246, n. 913, p. 295–305, 1953. 12

BALAN, N.; MARUYAMA, T.; PATRA, A.; NARAYANAN, V. A minimum in the latitude variation of spread F at march equinox. **Progress in Earth and Planetary Science**, v. 5, n. 1, p. 1–8, 2018. 32

BATISTA, I. S.; ABDU, M. Ionospheric variability at brazilian low and equatorial latitudes: comparison between observations and iri model. **Advances in Space Research**, v. 34, n. 9, p. 1894–1900, 2004. 65

BECKER-GUEDES, F.; SAHAI, Y.; FAGUNDES, P.; LIMA, W.; PILLAT, V.; ABALDE, J.; BITTENCOURT, J. Geomagnetic storm and equatorial spread F. In: **Annales Geophysicae**. [S.l.: s.n.], 2004. v. 22, n. 9, p. 3231–3239. 72

BERKNER, D. Irregularities in the equatorial ionosphere: the berkner symposium. **Reviews of Geophysics**, v. 12, n. 2, p. 285–289, 1930. 1

BERKNER, L.; WELLS, H. F region ionosphere-investigations at low latitudes. **Terrestrial Magnetism and Atmospheric Electricity**, v. 39, n. 3, p. 215–230, 1934. 1

BERTONI, F.; SAHAI, Y.; RAULIN, J.-P.; FAGUNDES, P.; PILLAT, V.; CASTRO, C. G. de; LIMA, W. Equatorial spread F occurrence observed at two near equatorial stations in the brazilian sector and its occurrence modulated by planetary waves. **Journal of Atmospheric and Solar-Terrestrial Physics**, v. 73, n. 4, p. 457–463, 2011. 28, 46

BILITZA, D. Iri the international standard for the ionosphere. **Advances in Radio Science**, v. 16, p. 1–11, 2018. 37

BOOKER, H.; WELLS, H. Scattering of radio waves by the F region of the ionosphere. **Terrestrial Magnetism and Atmospheric Electricity**, v. 43, n. 3, p. 249–256, 1938. 1

BREIT, G.; TUVE, M. A. A test of the existence of the conducting layer. **Physical Review**, v. 28, n. 3, p. 554, 1926. 1

CANDIDO. Spread F occurrence over a southern anomaly crest location in Brazil during june solstice of solar minimum activity. **Journal of Geophysical Research: Space Physics**, v. 116, n. A6, 2019. 34

CANDIDO, C.; BATISTA, I.; BECKER-GUEDES, F.; ABDU, M.; SOBRAL, J.; TAKAHASHI, H. Spread F occurrence over a southern anomaly crest location in Brazil during june solstice of solar minimum activity. **Journal of Geophysical Research: Space Physics**, v. 116, n. A6, 2011. 25

CHANDRA, H.; SHARMA, S.; ABDU, M.; BATISTA, I. Spread F at anomaly crest regions in the indian and american longitudes. **Advances in Space Research**, v. 31, n. 3, p. 717–727, 2003. 59

CHAPAGAIN, N. P.; FEJER, B. G.; CHAU, J. L. Climatology of postsunset equatorial spread F over jicamarca. **Journal of Geophysical Research: Space Physics**, v. 114, n. A7, 2009. 59

CHAPMAN, S. The electrical conductivity of the ionosphere: a review. **Il Nuovo Cimento (1955-1965)**, v. 4, n. 4, p. 1385–1412, 1956. 12

COWLEY, S. Magnetosphere-ionosphere interactions: a tutorial review. **Magnetospheric Current Systems, Geophysical Monograph Series**, v. 118, p. 91–106, 2000. 16

COWLING, T. G. The electrical conductivity of an ionized gas in a magnetic field, with applications to the solar atmosphere and the ionosphere. **Proceedings of the Royal Society of London. Series A. Mathematical and Physical Sciences**, v. 183, n. 995, p. 453–479, 1945. 12

DABAS, R.; DAS, R. M.; SHARMA, K.; GARG, S.; DEVASIA, C.; SUBBARAO, K.; NIRANJAN, K.; RAO, P. R. Equatorial and low latitude spread F irregularity characteristics over the indian region and their prediction possibilities. **Journal of Atmospheric and Solar-Terrestrial Physics**, v. 69, n. 6, p. 685–696, 2007. 59

DASHORA, N.; PANDEY, R. Observations in equatorial anomaly region of total electron content enhancements and depletions. **Annales Geophysicae**, v. 23, n. 7, p. 2449–2456, 2005. 28

DAVIES, K. **Ionospheric radio propagation**. [S.l.]: US Department of Commerce, National Bureau of Standards, 1965. 42

FARLEY, D.; BONELLI, E.; FEJER, B. G.; LARSEN, M. The prereversal enhancement of the zonal electric field in the equatorial ionosphere. **Journal of Geophysical Research: Space Physics**, v. 91, n. A12, p. 13723–13728, 1986. 20, 22, 62

FEJER, B. G.; SCHERLIESS, L.; PAULA, E. D. Effects of the vertical plasma drift velocity on the generation and evolution of equatorial spread F. **Journal of Geophysical Research: Space Physics**, v. 104, n. A9, p. 19859–19869, 1999. 60, 62, 72

FRITTS. Overview and summary of the Spread F Experiment (SpreadFEx). In: COPERNICUS GMBH. **Annales Geophysicae**. [S.l.], 2009. v. 27, n. 5, p. 2141–2155. 30

FRITTS, D. et al. Gravity wave and tidal influences on equatorial spread f based on observations during the Spread F Experiment (SpreadFEx). In: COPERNICUS GMBH. **Annales Geophysicae**. [S.l.], 2008. v. 26, n. 11, p. 3235–3252. 24

FUKUSHIMA, D.; SHIOKAWA, K.; OTSUKA, Y.; OGAWA, T. Observation of equatorial nighttime medium-scale traveling ionospheric disturbances in 630-nm airglow images over 7 years. **Journal of Geophysical Research: Space Physics**, v. 117, n. A10, 2012. 25

GONZALEZ, W.; JOSELYN, J.-A.; KAMIDE, Y.; KROEHL, H. W.; ROSTOKER, G.; TSURUTANI, B.; VASYLIUNAS, V. What is a geomagnetic storm? **Journal of Geophysical Research: Space Physics**, v. 99, n. A4, p. 5771–5792, 1994. 17, 39

GONZALEZ, W. D.; TSURUTANI, B. T. Criteria of interplanetary parameters causing intense magnetic storms (dst<- 100 nt). **Planetary and Space Science**, v. 35, n. 9, p. 1101–1109, 1987. 16

HANSOM, W.; CRAGIN, B.; DENNIS, A. The effect of vertical drift on the equatorial f-region stability. **Journal of Atmospheric and Terrestrial Physics**, v. 48, n. 3, p. 205–212, 1986. 56

HAYMES, R. **Introduction to space science**. Wiley, 1971. 1

HEELIS, R. Electrodynamics in the low and middle latitude ionosphere: a tutorial. **Journal of Atmospheric and Solar-Terrestrial Physics**, v. 66, n. 10, p. 825–838, 2004. 11, 13

HEELIS, R.; KENDALL, P.; MOFFETT, R.; WINDLE, D.; RISHBETH, H. Electrical coupling of the E and Fregions and its effect on F region drifts and winds. **Planetary and Space Science**, v. 22, n. 5, p. 743–756, 1974. 8, 10

HINES, C. O. Internal atmospheric gravity waves at ionospheric heights. **Canadian Journal of Physics**, v. 38, n. 11, p. 1441–1481, 1960. 24, 25

HUANG, C.-S.; KELLEY, M. C. Nonlinear evolution of equatorial spread F: 2. gravity wave seeding of rayleigh-taylor instability. **Journal of Geophysical Research: Space Physics**, v. 101, n. A1, p. 293–302, 1996. 26

KELLEY. **The Earth's ionosphere: plasma physics and electrodynamics**. [S.l.]: Academic press, 2009. 1, 5, 6, 7, 8, 21, 27

KELLEY, M. Equatorial spread F: recent results and outstanding problems. **Journal of Atmospheric and Terrestrial Physics**, v. 47, n. 8-10, p. 745–752, 1985. 55

KELLEY, M.; LARSEN, M.; LAHOZ, C.; MCCLURE, J. Gravity wave initiation of equatorial spread F: a case study. **Journal of Geophysical Research: Space Physics**, v. 86, n. A11, p. 9087–9100, 1981. 55

KELLEY, M. C. **The Earth's ionosphere: plasma physics and electrodynamics**. [S.l.]: Academic Press, 1989. 15, 19, 21, 27

KING, J. H. Solar wind parameters and magnetospheric coupling studies. **Solar Wind Magnetosphere Coupling**, v. 126, p. 163, 1986. 16

KOGA, D.; SOBRAL, J.; ABDU, M.; CASTILHO, V. de; MASCARENHAS, M.; ARRUDA, D.; ZAMLUTTI, C.; TAKAHASHI, H.; MEDEIROS, A.; BURITI, R. Space weather in the thermospheric–ionospheric domain over the brazilian region: climatology of ionospheric plasma bubbles in the subequatorial and low-latitude region. **Journal of Atmospheric and Solar-Terrestrial Physics**, v. 73, n. 11-12, p. 1529–1534, 2011. 2

KRALL, J.; HUBA, J.; FRITTS, D. On the seeding of equatorial spread F by gravity waves. **Geophysical Research Letters**, v. 40, n. 4, p. 661–664, 2013. 25

LAN, T.; JIANG, C.; YANG, G.; ZHANG, Y.; LIU, J.; ZHAO, Z. Statistical analysis of low-latitude spread F observed over Puer, China, during 2015–2016. **Earth, Planets and Space**, v. 71, n. 1, p. 1–9, 2019. 25

LEITINGER, R. e. a. The tid model for modulation of large scale electron density models. **Annals of Geophysics**, 2005. 24

LI, G.; NING, B.; ABDU, M.; YUE, X.; LIU, L.; WAN, W.; HU, L. On the occurrence of postmidnight equatorial F region irregularities during the june solstice. **Journal of Geophysical Research: Space Physics**, v. 116, n. A4, 2011. 33, 56, 62

LOCKWOOD, M. Reconstruction and prediction of variations in the open solar magnetic flux and interplanetary conditions. **Living Reviews in Solar Physics**, v. 10, n. 1, p. 1–88, 2013. 16

MA, A. Outstanding problems in the equatorial ionosphere–thermosphere electrodynamics relevant to spread F. **Journal of Atmospheric and Solar-Terrestrial Physics**, v. 63, n. 9, p. 869–884, 2001. 56

_____. Equatorial spread F development and quiet time variability under solar minimum conditions. **Indian Journal of Radio and Space Physics v.41, , p.168-183, 2012.**, 2012. 62

MACDOUGALL, J.; ABDU, M.; JAYACHANDRAN, P.; CECILE, J.-F.; BATISTA, I. Presunrise spread F at Fortaleza. **Journal of Geophysical Research: Space Physics**, v. 103, n. A10, p. 23415–23425, 1998. 56

OTSUKA, Y. Review of the generation mechanisms of post-midnight irregularities in the equatorial and low-latitude ionosphere. **Progress in Earth and Planetary Science**, SpringerOpen, v. 5, n. 1, p. 1–13, 2018. 28

OTSUKA, Y.; KOTAKE, N.; SHIOKAWA, K.; OGAWA, T.; TSUGAWA, T.; SAITO, A. Statistical study of medium-scale traveling ionospheric disturbances observed with a GPS receiver network in Japan. In: **Aeronomy of the Earth's Atmosphere and Ionosphere**. [S.l.: s.n.], 2011. p. 291–299. 25

OTSUKA, Y.; SUZUKI, K.; NAKAGAWA, S.; NISHIOKA, M.; SHIOKAWA, K.; TSUGAWA. Gps observations of medium-scale traveling ionospheric disturbances over europe. In: **Annales Geophysicae, v.26, n.11, p.3235-3252, 2008.** [S.l.: s.n.], 2013. v. 31, n. 2, p. 163–172. 25

PIGGOTT, W. R.; RAWER, K. **Ursi handbook of ionogram interpretation and reduction**. [s.l.]: NOAA, 1972. 1972. 27

PIMENTA, A.; KELLEY, M.; SAHAI, Y.; BITTENCOURT, J.; FAGUNDES, P. Thermospheric dark band structures observed in all-sky oi 630 nm emission images over the brazilian low-latitude sector. **Journal of Geophysical Research: Space Physics**, v. 113, n. A1, 2008. 25

RAGHAVARAO, R.; GUPTA, S.; SEKAR, R.; NARAYANAN, R.; DESAI, J.; SRIDHARAN, R.; BABU, V.; SUDHAKAR, V. In situ measurements of winds, electric fields and electron densities at the onset of equatorial spread-f. **Journal of Atmospheric and Terrestrial Physics**, v. 49, n. 5, p. 485–492, 1987. 22, 56

RASTOGI, R. Seasonal and solar cycle variations of equatorial spread F in the american zone. **Journal of Atmospheric and Terrestrial Physics**, v. 42, n. 7, p. 593–597, 1980. 60

RATCLIFFE, J. A. et al. **An introduction to ionosphere and magnetosphere**. [S.l.]: CUP Archive, 1972. 42

REINISCH. Automatic calculation of electron density profiles from digital ionograms: 3. processing of bottomside ionograms. **Radio Science**, v. 18, n. 3, p. 477–492, 1983. 41

REINISCH, B.; ANDERSON, D.; GAMACHE, R.; HUANG, X.; CHEN, C.; DECKER, D. Validating ionospheric models with measured electron density profiles. **Advances in Space Research**, v. 14, n. 12, p. 67–70, 1994. 46

REINISCH, B.; HUANG, X.; GALKIN, I.; PAZNUKHOV, V.; KOZLOV, A. Recent advances in real-time analysis of ionograms and ionospheric drift measurements with digisondes. **Journal of Atmospheric and Solar-Terrestrial Physics**, v. 67, n. 12, p. 1054–1062, 2005. 41, 44, 48, 71

REINISCH, B. W.; XUEQIN, H. Automatic calculation of electron density profiles from digital ionograms: 1. automatic o and x trace identification for topside ionograms. **Radio Science**, v. 17, n. 2, p. 421–434, 1982. 41

RISHBETH, H. The F layer dynamo. **Planetary and Space Science**, v. 19, n. 2, p. 263–267, 1971. 7, 9, 11

SEKAR, R.; RAGHAVARAO, R. Role of vertical winds on the rayleigh-taylor mode instabilities of the night-time equatorial ionosphere. **Journal of atmospheric and terrestrial physics**, v. 49, n. 10, p. 981–985, 1987. 21, 22

SOBRAL, J.; ABDU, M.; TAKAHASHI, H.; TAYLOR, M. J.; PAULA, E. D.; ZAMLUTTI, C.; AQUINO, M. D.; BORBA, G. Ionospheric plasma bubble climatology over brazil based on 22 years (1977–1998) of 630nm airglow observations. **Journal of Atmospheric and Solar-Terrestrial Physics**, v. 64, n. 12-14, p. 1517–1524, 2002. 2, 57, 59

TSUGAWA, T.; OTSUKA, Y.; COSTER, A.; SAITO, A. Medium-scale traveling ionospheric disturbances detected with dense and wide tec maps over North America. **Geophysical Research Letters**, v. 34, n. 22, 2007. 25

TSUNODA. On equatorial spread F: establishing a seeding hypothesis. **Journal of Geophysical Research: Space Physics**, v. 115, n. A12, 2010. 26

TSUNODA, R. T. Control of the seasonal and longitudinal occurrence of equatorial scintillations by the longitudinal gradient in integrated E region pedersen conductivity. **Journal of Geophysical Research: Space Physics**, v. 90, n. A1, p. 447–456, 1985. 59, 62

PUBLICAÇÕES TÉCNICO-CIENTÍFICAS EDITADAS PELO INPE

Teses e Dissertações (TDI)

Teses e Dissertações apresentadas nos Cursos de Pós-Graduação do INPE.

Notas Técnico-Científicas (NTC)

Incluem resultados preliminares de pesquisa, descrição de equipamentos, descrição e ou documentação de programas de computador, descrição de sistemas e experimentos, apresentação de testes, dados, atlas, e documentação de projetos de engenharia.

Propostas e Relatórios de Projetos (PRP)

São propostas de projetos técnico-científicos e relatórios de acompanhamento de projetos, atividades e convênios.

Publicações Seriadas

São os seriados técnico-científicos: boletins, periódicos, anuários e anais de eventos (simpósios e congressos). Constam destas publicações o Internacional Standard Serial Number (ISSN), que é um código único e definitivo para identificação de títulos de seriados.

Pré-publicações (PRE)

Todos os artigos publicados em periódicos, anais e como capítulos de livros.

Manuais Técnicos (MAN)

São publicações de caráter técnico que incluem normas, procedimentos, instruções e orientações.

Relatórios de Pesquisa (RPQ)

Reportam resultados ou progressos de pesquisas tanto de natureza técnica quanto científica, cujo nível seja compatível com o de uma publicação em periódico nacional ou internacional.

Publicações Didáticas (PUD)

Incluem apostilas, notas de aula e manuais didáticos.

Programas de Computador (PDC)

São a seqüência de instruções ou códigos, expressos em uma linguagem de programação compilada ou interpretada, a ser executada por um computador para alcançar um determinado objetivo. Aceitam-se tanto programas fonte quanto os executáveis.